Cell

Proteomics of Melanoma Response to Immunotherapy Reveals Mitochondrial Dependence

Graphical Abstract

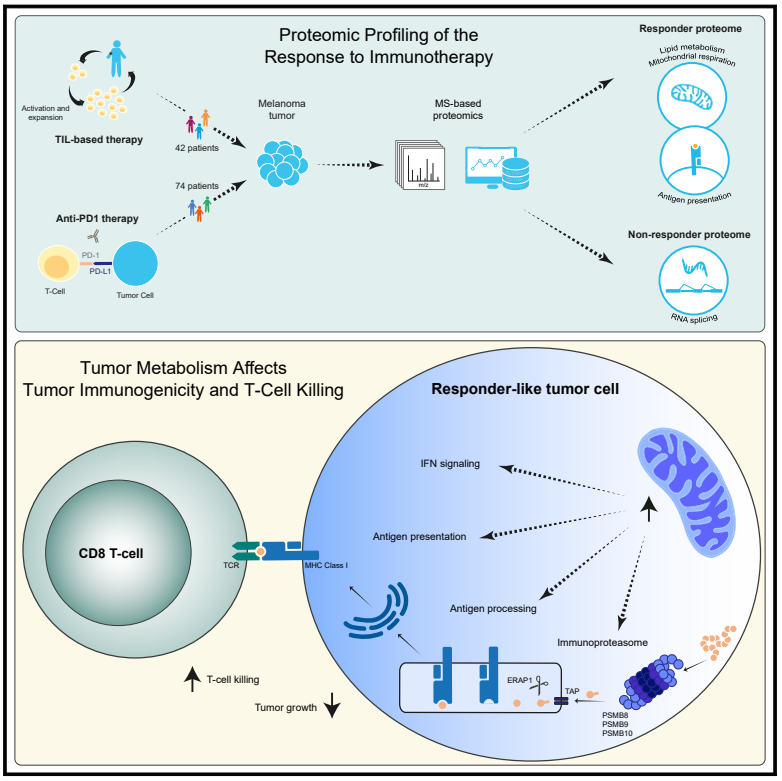

Highlights

- Proteomics of 116 melanoma tumors shows the landscapes of response to immunotherapy
- Immunotherapy response was associated with enriched mitochondrial lipid metabolism
- High mitochondrial metabolism led to higher antigen presentation and IFN signaling
- Knockout of beta-oxidation genes reduced melanoma sensitivity to T cell killing

Authors

Michal Harel, Rona Ortenberg, Siva Karthik Varanasi, ..., Susan M. Kaech, Gal Markel, Tamar Geiger

Correspondence

markel@post.tau.ac.il (G.M.), geiger@tauex.tau.ac.il (T.G.)

In Brief

Proteomic profiling of melanomas from patients undergoing immunotherapy reveals key mediators of tumor immunogenicity.

Harel et al., 2019, Cell *179*, 236–250
September 19, 2019
https://doi.org/10.1016/j.cell.2019.08.012

CellPress

Cell

Resource

Proteomics of Melanoma Response to Immunotherapy Reveals Mitochondrial Dependence

Michal Harel,[1] Rona Ortenberg,[2,3] Siva Karthik Varanasi,[4] Kailash Chandra Mangalhara,[5] Mariya Mardamshina,[1] Ettai Markovits,[2,3] Erez N. Baruch,[2,3] Victoria Tripple,[4] May Arama-Chayoth,[1] Eyal Greenberg,[2] Anjana Shenoy,[1] Ruveyda Ayasun,[4] Naama Knafo,[1] Shihao Xu,[4] Liat Anafi,[6] Gali Yanovich-Arad,[1] Georgina D. Barnabas,[1] Shira Ashkenazi,[2,3] Michal J. Besser,[2,3] Jacob Schachter,[2,7] Marcus Bosenberg,[8,9,10] Gerald S. Shadel,[5] Iris Barshack,[6,7] Susan M. Kaech,[4] Gal Markel,[2,3,*] and Tamar Geiger[1,11,*]

[1]Department of Human Molecular Genetics and Biochemistry, Sackler School of Medicine, Tel Aviv University, Tel-Aviv 6997801, Israel
[2]Ella Lemelbaum Institute of Immuno-Oncology, Sheba Medical Center, Tel Hashomer 5265601, Israel
[3]Department of Clinical Immunology and Microbiology, Sackler School of Medicine, Tel Aviv University, Tel-Aviv 6997801, Israel
[4]NOMIS Center for Immunobiology and Microbial Pathogenesis, Salk Institute for Biological Studies, La Jolla, CA 92037, USA
[5]Salk Institute for Biological Studies, La Jolla, CA 92037, USA
[6]Institute of Pathology, Sheba Medical Center, Tel Hashomer 5265601, Israel
[7]The Sackler School of Medicine, Tel Aviv University, Tel-Aviv 6997801, Israel
[8]Department of Pathology, Yale University School of Medicine, New Haven, CT 06510, USA
[9]Yale Comprehensive Cancer Center, New Haven, CT 06510, USA
[10]Department of Dermatology, Yale University School of Medicine, New Haven, CT 06510, USA
[11]Lead Contact
*Correspondence: markel@post.tau.ac.il (G.M.), geiger@tauex.tau.ac.il (T.G.)
https://doi.org/10.1016/j.cell.2019.08.012

SUMMARY

Immunotherapy has revolutionized cancer treatment, yet most patients do not respond. Here, we investigated mechanisms of response by profiling the proteome of clinical samples from advanced stage melanoma patients undergoing either tumor infiltrating lymphocyte (TIL)-based or anti- programmed death 1 (PD1) immunotherapy. Using high-resolution mass spectrometry, we quantified over 10,300 proteins in total and ~4,500 proteins across most samples in each dataset. Statistical analyses revealed higher oxidative phosphorylation and lipid metabolism in responders than in non-responders in both treatments. To elucidate the effects of the metabolic state on the immune response, we examined melanoma cells upon metabolic perturbations or CRISPR-Cas9 knockouts. These experiments indicated lipid metabolism as a regulatory mechanism that increases melanoma immunogenicity by elevating antigen presentation, thereby increasing sensitivity to T cell mediated killing both *in vitro* and *in vivo*. Altogether, our proteomic analyses revealed association between the melanoma metabolic state and the response to immunotherapy, which can be the basis for future improvement of therapeutic response.

INTRODUCTION

Immunotherapy has revolutionized the treatment of metastatic melanoma patients, achieving dramatic improvement of patient survival. So far, this success has largely been attributed to the high mutational load of melanoma. Immune checkpoint inhibitors (ICIs) are currently considered the mainstay of melanoma immunotherapy, particularly antibodies targeting either the cytotoxic T-lymphocyte-associated protein 4 (CTLA-4) or the programmed death 1 (PD1) immune checkpoints, yet approximately 50% of the patients do not respond to treatment (Hodi et al., 2010; Robert et al., 2011; Schadendorf et al., 2015; Topalian et al., 2012). Adoptive cell transfer (ACT) of tumor-infiltrating lymphocytes (TILs) is a different immunotherapeutic strategy that shows high efficacy in melanoma treatment (Dudley et al., 2005; Rosenberg et al., 1988). In the pre-anti-PD1 era, our team and others have shown that TIL-based therapy overcomes the limited immune activity and elicits around 50% response rates (Besser et al., 2010; Dudley et al., 2005; Radvanyi et al., 2012; Zikich et al., 2016).

Prognostic biomarkers for melanoma rely mostly on baseline clinical and pathological features, such as ratios between intratumoral immune cell sub-populations or plasma lactate dehydrogenase (LDH) levels (Weide et al., 2016). Beyond prognostic markers, much effort has been invested into the identification of predictive response markers and unraveling resistance mechanisms, predominantly using histological and genomic approaches (Pitt et al., 2016; Wellenstein and de Visser, 2018). Parameters such as expression of checkpoint proteins, mutational load, neoepitope load, T cell receptor clonality, and immune gene signatures correlate with response rate, but largely overlap between responders and non-responders, and are therefore of low predictive value (Gibney et al., 2016). Recent "omics" studies focused on finding transcriptomic signatures of response. Cytolytic markers (Van Allen et al., 2015) and immune-related gene signatures (Auslander et al., 2018; Ayers et al., 2017; Lauss et al., 2017; Riaz et al., 2017) were associated with response in different therapy approaches. Hugo et al. (2016) established innate PD1 resistance signature (IPRES), which is

comprised of mesenchymal transition-related genes, extracellular matrix modulators, hypoxia regulators, and angiogenesis factors. More recently, Cascone and colleagues found that elevated glycolysis increases resistance to TIL-based therapy (Cascone et al., 2018). The field of single-cell RNA-sequencing (scRNA-seq) has lately profiled tumor sub-populations, showing that melanoma cells display heterogeneity in their transcriptional programs (Tirosh et al., 2016), whereas non-responder cells express a resistance program controlled by CDK4 and CDK6 (Jerby-Arnon et al., 2018). Others have studied $CD8^+$ T cell sub-populations and their association with response, showing that T cells expressing transcription factor 7 (TCF-7) are correlated with response (Sade-Feldman et al., 2017), whereas a subset of dysfunctional $CD8^+$ cells are regulated by intracellular metallothioneins (Singer et al., 2016), and display a continuous progression from an early effector into a dysfunctional T cell state (Li et al., 2018).

In contrast to the extensive transcriptomics research, deep proteomic analysis of melanoma has not yet been performed. We and others have shown that there are major differences between these two regulatory layers (Vogel et al., 2010; Wang et al., 2017a) that can have major implications on cancer classification and biomarker identification (Mertins et al., 2016; Yanovich et al., 2018). In addition, the proteomic layer reflects much more accurately the cellular function. We therefore chose to examine melanoma immunotherapy response by using high-resolution liquid chromatography-mass spectrometry (LC-MS/MS)-based proteomics, aiming to identify signatures and cellular mechanisms of immunotherapy response. To that end, we assembled two cohorts of patients treated with TIL or anti-PD1. Analysis of a total of 116 patients revealed major functional differences between responders and non-responders to both treatments, specifically involving oxidative and lipid metabolism along with antigen presentation. *In vitro* and *in vivo* functional analyses revealed that lipid and ketone body metabolism proteins in the cancer cells are major mediators of antigen presentation and tumor immunogenicity.

RESULTS

Proteomic Analysis of Melanoma Response to TIL and Anti-PD1

Aiming to identify protein networks associated with response to immunotherapy, we assembled a cohort of 116 stage IV melanoma samples, including 42 patients treated with TIL and 74 patients treated with anti-PD1, and performed untargeted MS-based proteomic analysis. We divided each cohort into two main groups of responders (including partial and complete responders; n = 61) and non-responders (progressive disease; n = 48). The PD1 cohort included additional patients with stable disease (n = 7) (Figure 1A; Table S1A). Examination of the patients' clinical parameters showed that responders and non-responders present highly significant differences in overall survival (Figure 1B). Both the age and *BRAF* mutation status showed no significant difference between the groups. Additionally, prior treatments with targeted therapy (n = 16) or anti-CTLA-4 (n = 29) showed no association with response. In agreement with previous reports (Conforti et al., 2018), in the TIL cohort we found significant association with gender (Figures S1A–S1C), and lower plasma LDH levels were found in the responders than in non-responders of both cohorts (p value < 0.005; Chi square test) (Figures S1A–S1C), as previously reported (Weide et al., 2016). In accordance with (Besser et al., 2013), in the TIL cohort the number of infused CD8 cells was found to be the most significant predictor (p value = 3.19E−04; Student's t test); however, this parameter is available only after TILs have been extracted and propagated *ex vivo*, which limits its use.

For proteomic analysis, we dissected melanoma regions with > 80% tumor cells and followed with stable isotope labeling with amino acids in cell culture (SILAC)-based high-resolution LC-MS/MS analysis. To obtain accurate proteome quantification, we designed a super-SILAC mix, which was composed of five SILAC-labeled melanoma cell lines that served as a reference for normalization (Geiger et al., 2010). Examination of the ratios of the super-SILAC standard toward the tumor proteins showed high concordance, reflecting its suitability as an internal standard (Figure S1D). The mix was then spiked into each of the melanoma samples at a 1:1 protein ratio to serve as the reference for quantification. The combined protein lysates were trypsin-digested and fractionated, followed by high-resolution LC-MS/MS analysis on the Q-Exactive Plus or HF mass spectrometers (Figure 1C). Overall, 10,376 non-redundant protein groups were quantified (with 1% false discovery rate [FDR] on the peptide and protein levels) (Table S1B); there were no major differences in the coverage between the responders and non-responders (Figures 1D–1E). All downstream statistical analyses were performed upon further data filtration to retain only proteins identified in at least 70% of the samples. These lists, of 4,400–4,600 proteins (Tables S1C and S1D), included more than 800 signal-transduction-related proteins and dozens of receptors and transcription-factor-associated proteins, indicating sufficient coverage for analysis of intracellular processes (Table S1E).

Functional Analysis of Responders and Non-responders to Immunotherapy

Initial bioinformatic analysis examined the functional differences between responders and non-responders in each therapy. We first applied a low stringency Student's t tests with a nominal p value cutoff (p value < 0.05) and found 414 and 636 differentially expressed proteins (DEPs) in the TIL and the anti-PD1 cohorts, respectively (Tables S2A and S2B). We then constructed proteomaps to cluster the DEPs according to their Kyoto Encyclopedia Genes and Genomes (KEGG) pathway annotations and found a striking resemblance between the maps of the two treatments (Figures 2A and S2A). In both, the responder group was dominated by higher levels of metabolic proteins, whereas non-responders were dominated by spliceosome and RNA-metabolism-related proteins. Along with the metabolic categories, responders from both datasets had higher proportions of antigen-presentation-related proteins, as well as signaling-related categories (mitogen-activated protein kinase [MAPK], nuclear factor-κB [NF-κB], and RAS signaling pathways), all of which play important roles in melanoma and in the response to immunotherapy (Manguso et al., 2017; Sumimoto et al., 2006). In agreement with the high pathway resemblance between the two therapies, a two-dimensional (2D) annotation enrichment test

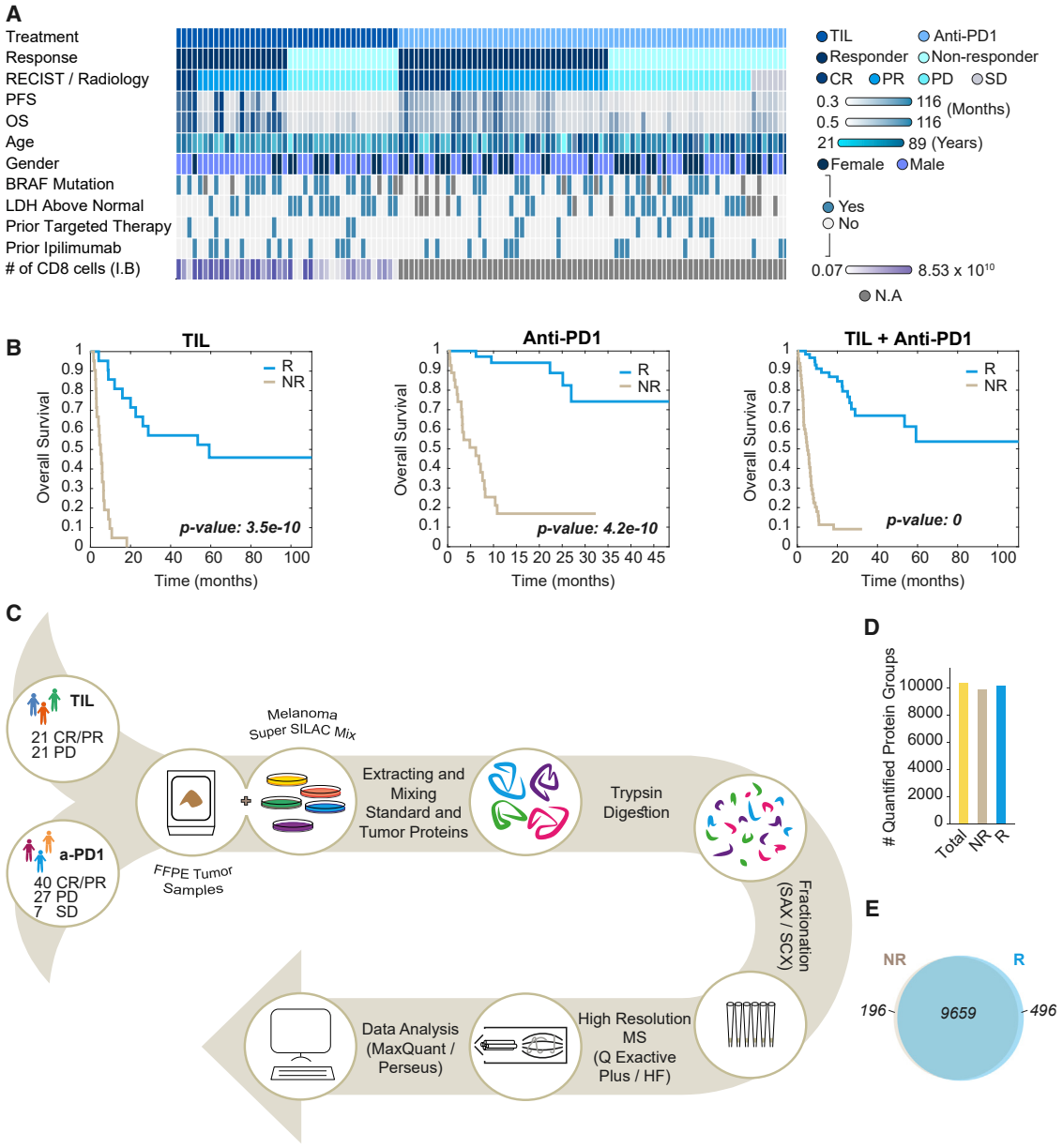

Figure 1. Proteomics of Melanoma Response to Immunotherapy

(A) The study cohort includes 42 and 74 patients undergoing TIL-based or anti-PD1 immunotherapy, respectively. Clinical parameters are indicated in the heatmap. See also Figures S1A–S1C and Table S1A.

(B) Kaplan-Meier plots show highly significant differences between responders and non-responders to TIL or anti-PD1 treatments in overall survival (OS). See also Table S1A.

(C) The proteomics workflow involved protein extraction from FFPE tissues and mixing with a super-SILAC standard. The proteins were then trypsin-digested, followed by peptide fractionation. We used liquid chromatography coupled with the Q Exactive Plus or Q Exactive HF MS followed by computational analysis in MaxQuant and Perseus.

(D) Total number of proteins quantified in each group of samples.

(E) A Venn diagram showing the overlap of quantified proteins in each group. Abbreviations are as follows: CR, complete response; PR, partial response; PD, progressive disease; SILAC, stable isotope labeling with amino acids in cell culture; NR, non-responders (including PD); R, responders (including CR and PR); IB, infusion bag.

distribution displayed a high overall correlation between the enriched categories in both treatments (R = 0.76; p value = 1.5E−86). In both treatments, responders were significantly enriched for mitochondrial metabolic pathways, including the tricarboxylic acid (TCA) cycle, fatty acid oxidation, and ketone body metabolism (2D annotation enrichment analysis, FDR

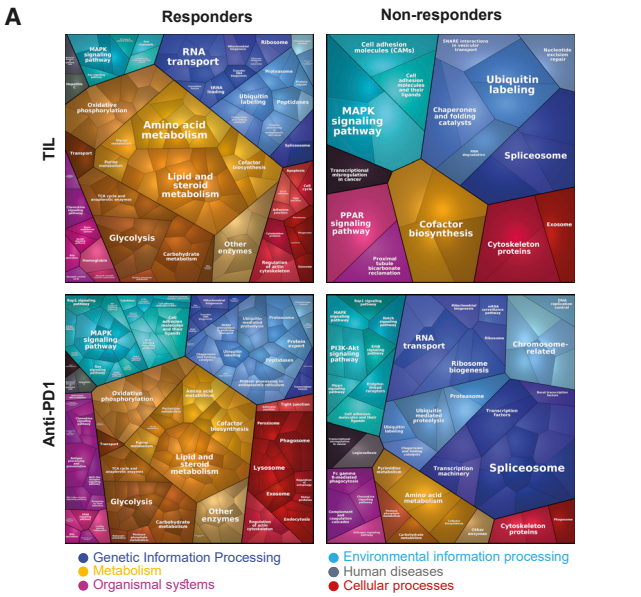

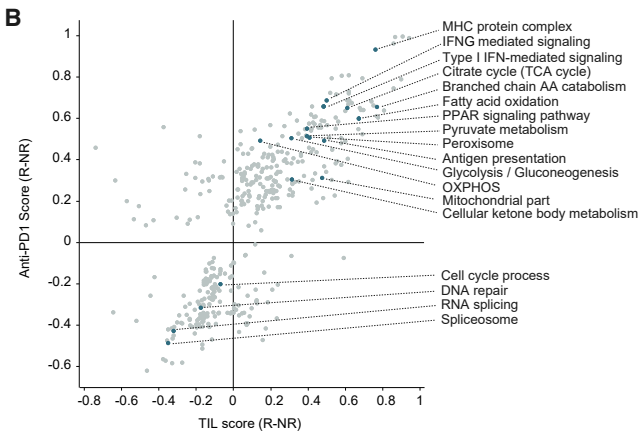

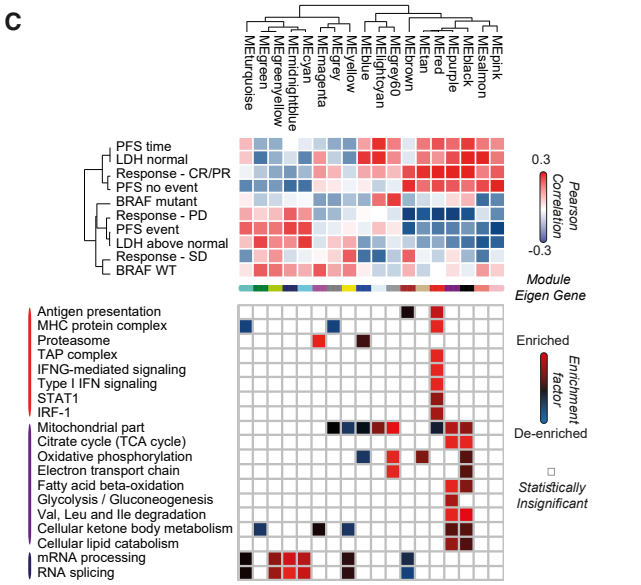

Figure 2. Functional Differences between Responders and Non-responders to Immunotherapy

(A) Functional categories higher in responders (left) and non-responders (right), as illustrated by using Proteomaps (Liebermeister et al., 2014). Each polygon corresponds to a single KEGG pathway, and the size correlates with the ratio between the groups. The maps show high similarity between the KEGG pathways of DEPs upon TIL and anti-PD1 treatments. See also Figure S2A and Tables S2A and S2B.

(B) Two-dimensional annotation enrichment analysis shows similar enrichments in the two immunotherapy regimens (FDR q value < 0.02). In both treatments, responders are enriched with mitochondrial metabolism-related pathways and antigen presentation related categories, whereas non-responders are enriched with mRNA processing pathways and cell cycle proteins. See also Table S2C.

(C) WGCNA of 116 melanoma samples shows module eigengenes (MEs) highly correlated with long PFS and CR or PR classification (upper heatmap). Enrichment analysis for the different MEs is presented in the lower heatmap (FDR q value < 0.05). See also Table S2D.

q value < 0.02) (Figure 2B; Table S2C). These processes concurred with enrichment of antigen presentation and type I and type II interferon (IFN) signaling categories. The non-responder group was significantly associated with cell cycle, in accordance with Lauss et al. (2017), as well as with splicing-related categories.

Given the functional similarity of the response profiles to both treatments, we searched for common functional determinants associated with the patient clinical parameters. We integrated the two cohorts to create a single dataset of all 116 samples and performed weighted gene correlation network analysis (WGCNA). Separation of the proteomic profiles to eigengene modules identified a group of modules that were positively associated with patient progression-free survival, complete or partial response, and normal plasma LDH level. In agreement with the previous results, these modules showed enrichment of antigen presentation and IFNG signaling along with mitochondrial metabolic pathways (Fisher exact test, FDR *q*-value < 0.05) (Figure 2C; Table S2D). WGCNA further revealed an association between *BRAF* mutation and elevated levels of mitochondrial OXPHOS proteins, but no association with response, whereas WT *BRAF* was associated with higher expression of RNA splicing and RNA processing and SD samples, implying that there could be another level of complexity.

To examine the generality of the mitochondria-IFN association, we compared our results to published RNA-seq datasets that explored the response to anti-PD1- (Hugo et al., 2016), anti-CTLA-4- (Van Allen et al., 2015), and TIL-based (Lauss et al., 2017) treatments. Enrichment analysis showed that responders in all three datasets had moderately higher levels of mitochondrial genes than did non-responders, including OXPHOS TCA cycle and ketone body metabolism, along with antigen presentation and type I and type II IFN signaling pathway genes. Fatty acid catabolism was enriched in responders of two of the three RNA datasets (2D annotation enrichment test, FDR q value < 0.05) (Figure S2B; Tables S2E–S2G). Comparison to the proteomic data shows that the metabolic enrichment was much lower at the RNA level than at the proteome level, whereas the antigen-presentation- and IFN-related categories were enriched to the same extent. Altogether, these analyses highlight that differences in mitochondrial metabolism are generally associated with immunotherapeutic response, irrespective of the treatment regimen, and are evident at the RNA level as well, though to a much lower extent than at the proteome level.

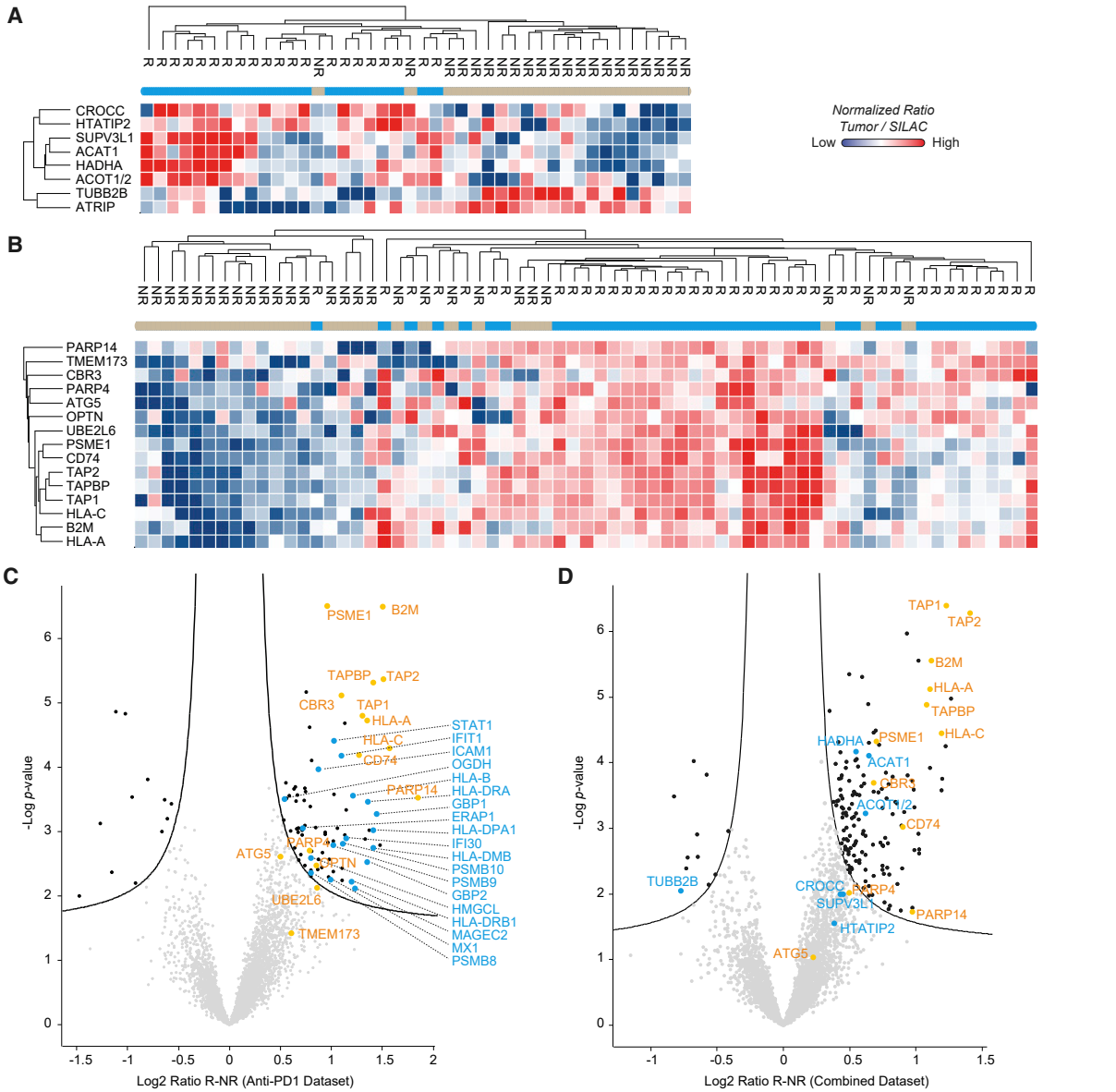

Figure 3. Protein Signatures of Response to Immunotherapy

(A) Heatmap of the TIL signature shows eight proteins that discriminate between responders and non-responders. TUBB2B and ATRIP are more highly expressed in non-responders than in responders, and CROCC, HTATIP2, SUPV3L1, ACAT1, HADHA, and ACOT1 or ACOT2 are higher in responders than in non-responders. See also Figures S3A and S3B.

(B) Heatmap of anti-PD1 signature shows 15 proteins that discriminate between responders and non-responders, all of them higher in the responders. See also Figure S3C and S3D.

(C) A volcano plot shows the results of a Student's t test comparing responders and non-responders to anti-PD1 (FDR q value < 0.1, S0 = 0.1). Signature proteins are in orange. Additional selected proteins are in blue. See also Table S4A.

(D) A volcano plot that shows the results of a Student's t test between responders and non-responders in the integrated cohort of TIL- and anti-PD1-treated samples (FDR q value < 0.1, S0 = 0.1). Blue proteins are the TIL signature and orange proteins are the anti-PD1 signature. See also Table S4B.

Identification of Protein Markers of Response to Immunotherapy

Aiming to reduce the broad pathway view to specific proteins and identify minimal protein signatures of response, we applied support vector machine (SVM)-based classification with ANOVA-based feature selection embedded in a recursive cross validation procedure (see STAR Methods). For the TIL cohort, this procedure resulted in an eight-protein signature; six of those were higher and two were lower in the responders than in non-responders (Figure 3A). The signature provided excellent separation between the groups according to the first component in the principal component analysis

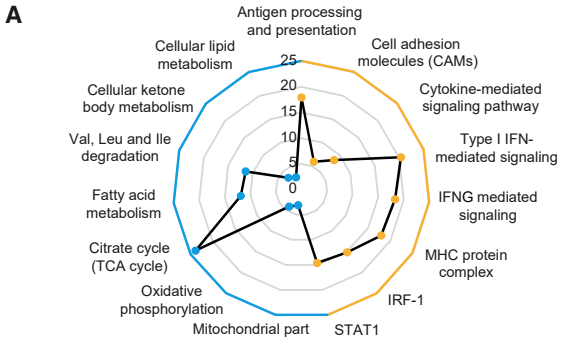

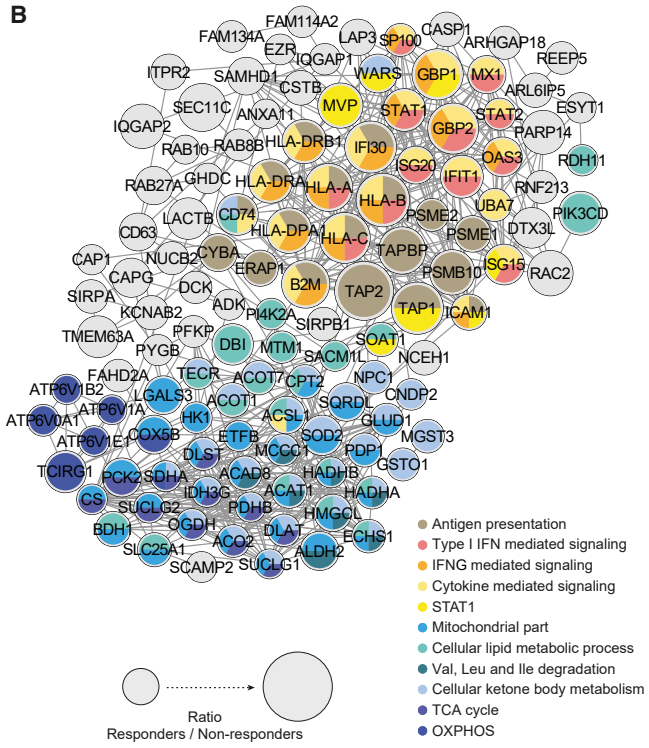

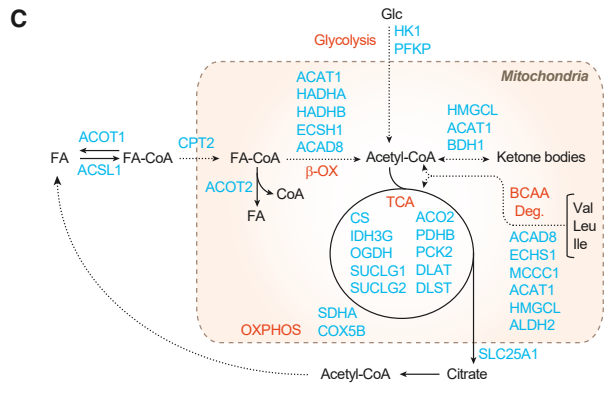

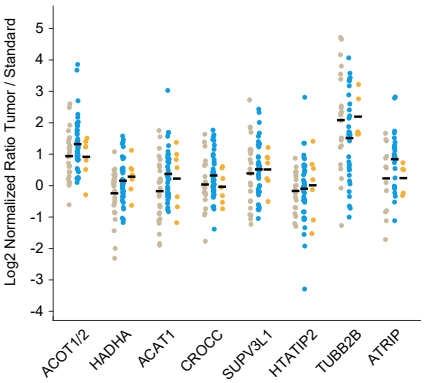

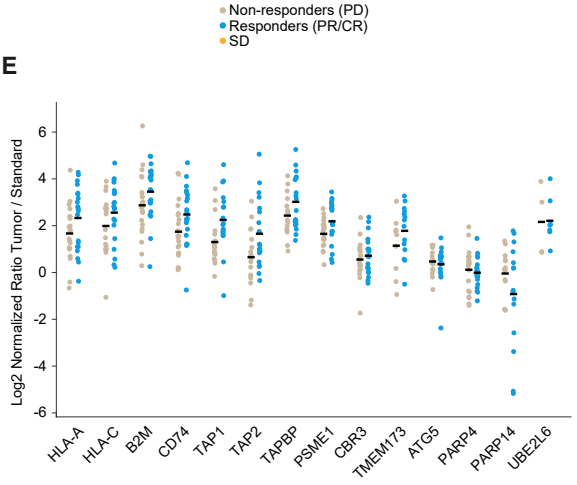

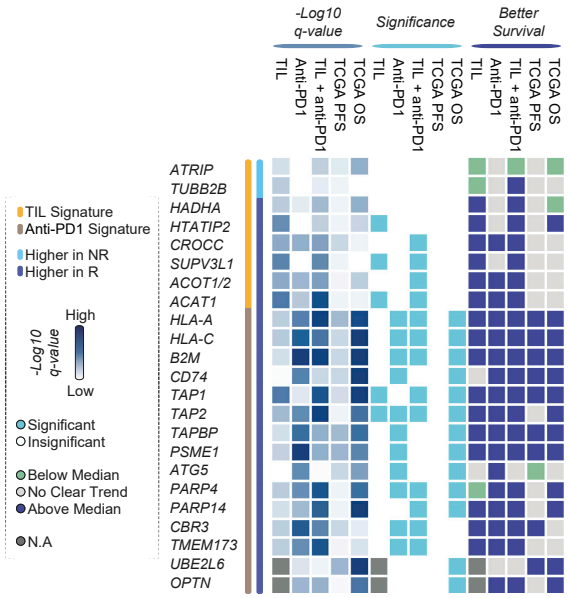

(legend on next page)

(PCA) (Figure S3A), and the receiver operating characteristics (ROCs) curve showed high sensitivity and specificity of prediction with an area under the curve (AUC) of 0.85 (Figure S3B). The same procedure applied to the anti-PD1 cohort resulted in a 15-protein signature, all higher in the responder group than in the non-responder group with an AUC of the ROC curve of 0.77 (Figures 3B, S3C, and S3D). Comparing the two signatures showed that, despite the high-functional similarity between the response profiles of both treatments, there was no overlap between them. The TIL cohort included proteins related to fatty acid and ketone body metabolism, ACOT1/ACOT2, ACAT1, and HADHA. The anti-PD1 signature was comprised of multiple antigen-presentation-related proteins, including the major histocompatibility complex (MHC) class I molecules (human leukocyte antigen [HLA]-A, HLA-C, and B2M), MHC class II chaperone CD74, antigen peptide transporters (TAP1 and TAP2), TAPBP (which mediates the interactions between the HLAs and the peptide transporters), and the proteasomal subunit PSME1. Of note, when running the algorithm on the TIL dataset combined with selected baseline clinical information, the only feature that outperformed the proteomics classifiers was the number of CD8 cells in the infusion bag. The next ranked clinical feature, plasma LDH level, was much inferior to the signature proteins in both the TIL and the anti-PD1 datasets (Tables S3A and S3B).

Statistical analysis of the anti-PD1 cohort showed that 12 proteins out of 15 PD1-signature proteins were also statistically significant (Student's t test; permutation-based FDR q value < 0.1, S0 = 0.1) (Figure 3C; Table S4A). In total, we found 95 significantly changing proteins in the PD1 cohort, 83 of them higher in the responders than in non-responders, including 4 MHC class II proteins, all 3 immunoproteasome subunits (PSMB8, PSMB9, and PSMB10), ERAP1 (an aminopeptidase that generates most of the HLA peptides), STAT1, as well as multiple metabolic enzymes. Due to the smaller size of the TIL cohort, there were no significantly changing proteins. To increase the statistical power of the analysis, we merged the two cohorts and followed with a Student's t test (permutation-based FDR q value < 0.1, S0 = 0.1) (Table S4B). We found 160 significantly changing proteins between the responders and non-responders, including 10 of the PD1 signature (primarily MHC-related) and 3 of the TIL signature proteins (ACAT1, ACOT1/ACOT2, and HADHA) (Figure 3D). Construction of a protein interaction network of the responder proteins showed two highly connected protein clusters; the first was enriched with the IFN and antigen processing and presentation machinery proteins; the second was enriched with mitochondrial metabolic enzymes involved in lipid metabolism and TCA cycle (Fisher exact test, q value < 0.02) (Figures 4A–4C and S4A; Table S4C). Thus, the mitochondria-IFN network is associated with response to both treatments, despite the fact that the proteins do not necessarily predict response in both cases. In agreement, examination of the TIL signature on the anti-PD1 cohort data showed that the general trend of most proteins is similar between the cohorts. All six responder proteins of the TIL signature were also upregulated in the anti-PD1 responders (Figure 4D). Similarly, examination of the anti-PD1 signature on the TIL cohort showed a similar trend for 10 of the 15 proteins. Importantly, the MHC-related proteins (HLA-A, HLA-C, B2M, and CD74) and the antigen presentation machinery proteins (TAP1, TAP2, TAPBP, and PSME1) were all higher in the TIL responders than in non-responders (Figure 4E).

Next, we validated the clinical significance of the signature proteins and associated their expression levels with progression-free survival (PFS). Kaplan Meier analysis showed that above-median expression levels of ACAT1, SUPV3L1, and HTATIP2 were associated with longer PFS in the TIL cohort (Benjamini Hochberg FDR q value < 0.05) (Figure 4F). Interestingly, there was no such association for RNA expression in The Cancer Genome Atlas (TCGA) data for any of the TIL signature proteins. In agreement, examination of the signature gene expression in the immunotherapy transcriptomics datasets, most genes showed similar trends, but much milder differences than the proteomics data (Figures S4B and S4C). In the anti-PD1 cohort, most of the signature proteins were significantly associated with longer PFS, and this was also evident in the TCGA overall survival data. Analysis of each signature protein on the other cohort showed almost no association with survival (Figure 4F). The association between the anti-PD1 signature and the TCGA survival data show that antigen presentation signal is associated with tumor aggressiveness and immune evasion, irrespective of the patient treatment course. Discrepancies with the TIL results might be associated with the high variability of the TCGA cohort (e.g., prior treatments and disease stage), which could affect cancer cell metabolism. In addition, our results show lower consistency between the protein and RNA signals of these proteins, suggesting that the TCGA gene expression data is unlikely to reflect the protein levels, as measured in the current study.

The proteomic results correlated the melanoma metabolic state with antigen presentation and IFN signaling. Given that these analyses might have averaged signals from different cell populations, we examined the spatial expression of key signature proteins on the tissue level by immunohistochemistry of consecutive slides. We focused on the three metabolic proteins from the TIL signature, ACAT1, ACOT1, and HADHA. In addition, we stained for micropthalmia transcription factor (MITF) to mark

Figure 4. Integrated Analysis of Response to Immunotherapy

(A) Enrichment analysis of selected processes higher in the responders to immunotherapy from the joint TIL-PD1 dataset (FDR q value < 0.2). Radial plot indicates the enrichment factor. The entire list of enriched processes is in Table S4C.

(B) Protein-protein interaction network of the significantly upregulated proteins in the responders to immunotherapy in the combined dataset. The node size correlates with the ratio between responders and non-responders. Enriched KEGG pathways are colored as indicated. See also Table S4B.

(C) Schematic representation of the metabolic pathways of proteins significantly higher in the responder group.

(D) Dot plot shows the changes in the TIL signature proteins in the anti-PD1 cohort data.

(E) Dot plot of the anti-PD1 signature proteins on the TIL cohort data.

(F) Kaplan-Meier analyses of both signatures on each proteomics cohort separately, the integrated proteomics cohort of 109 samples (excluding SD), and the TCGA mRNA melanoma dataset (Cancer Genome Atlas Network, 2015). Heatmap indicates the −log q value, the significance (q value < 0.05), and the Kaplan-Meier directionality with respect to expression (below or above median). Abbreviations are as follows: OS, overall survival; PFS, progression free survival.

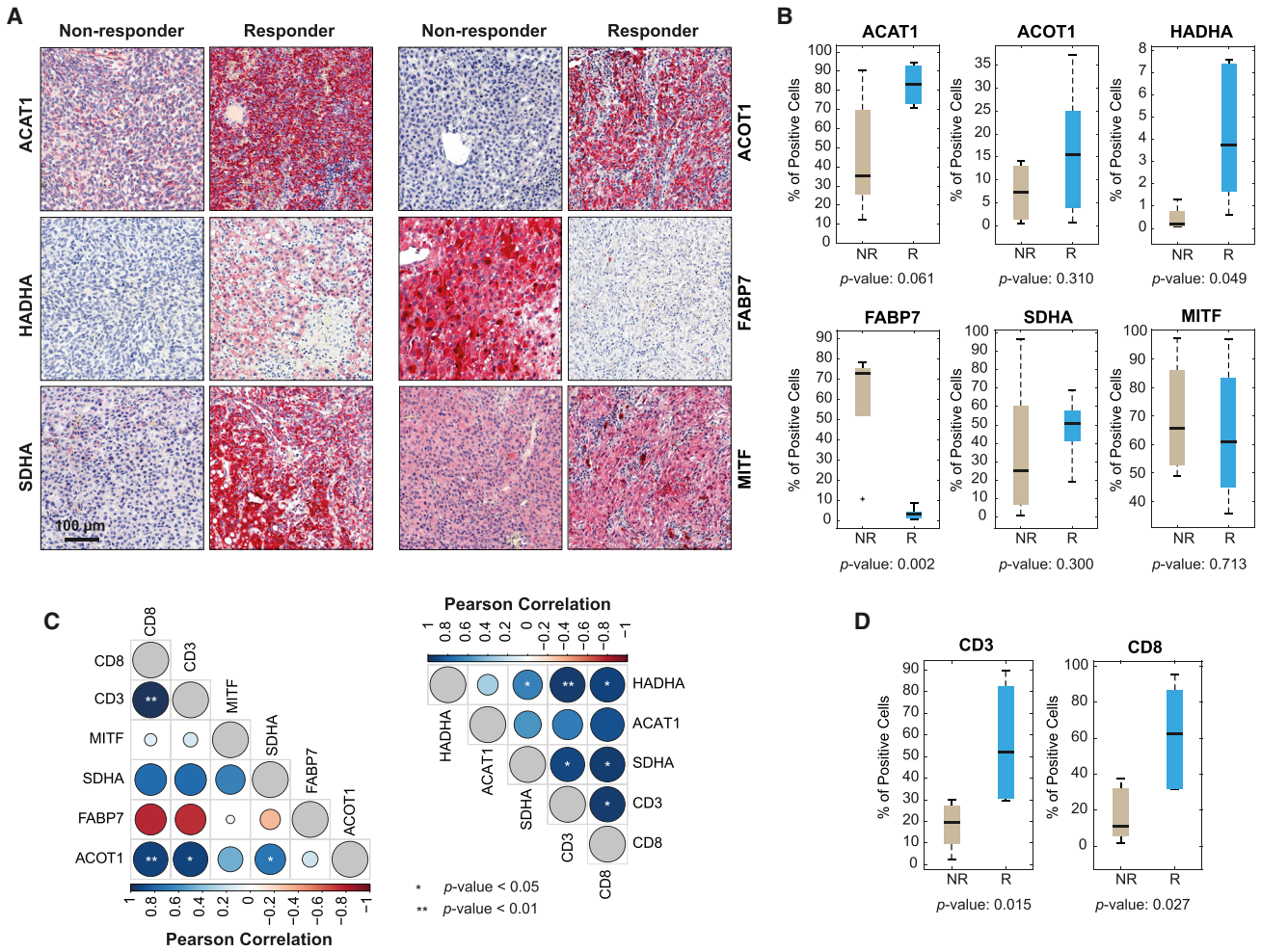

Figure 5. Tissue-Level Validation of the Metabolic Proteins and T Cell Infiltration

(A) IHC of selected metabolic proteins from the TIL signature: ACAT1, ACOT1, and HADHA. MITF is used as a melanoma marker. SDHA is used as a mitochondrial marker. FABP7 is a melanoma antigen that shows an opposite trend in the TIL proteomics data. Scale bar, 100 μm.

(B) Boxplots show the quantification of the IHC results.

(C) Correlation heatmap of IHC-stained proteins. *p < 0.05; **p < 0.1.

(D) Boxplots for the quantification of CD3 and CD8 cells. See also Figure S5.

the melanoma cells, and fatty acid binding protein 7 (FABP7), which is a known melanoma antigen (Goto et al., 2010) that was lower in the TIL responder group than in the non-responder group. Immunostaining showed significant differences in expression between the responders and non-responders, in agreement with the proteomics data, and showed specific staining of signature proteins in the melanoma cells rather than the stroma (Figures 5A and 5B). Staining of the mitochondrial marker and electron transport chain (ETC) component succinate dehydrogenase complex flavoprotein subunit A (SDHA) showed an overall significant increase in mitochondria in the responders, albeit to a lower extent than the signature proteins (Figure 5C). We then examined the association between the metabolic protein expression and T cell infiltration (Figures 5C, 5D, S5A, and S5B). In agreement with the higher treatment efficacy in these patients, we found high correlation between CD8 or CD3 T cell staining and the signature proteins ACOT1, ACAT1, and HADHA (Figure 5C). Lower correlation was found with SDHA, and we found no correlation with MITF. Altogether, these results prove that there is a clear link between tumor mitochondrial metabolism and the cellular immunogenicity, which warrant downstream functional investigation.

Functional Validation of Metabolic Regulation of Melanoma Cell Immunogenicity

Beyond the correlation between the metabolic profiles and the immune response, we asked whether there is also a functional role of mitochondrial metabolism in increasing tumor immunogenicity. To induce increased mitochondrial respiration in cell culture, we treated four melanoma cell lines with dichloroacetate (DCA), an inhibitor of pyruvate dehydrogenase kinase, which elevates the carbon flux into the mitochondria. Proteomic analysis of DCA-treated cells showed increased expression of multiple proteins involved in antigen presentation, including the

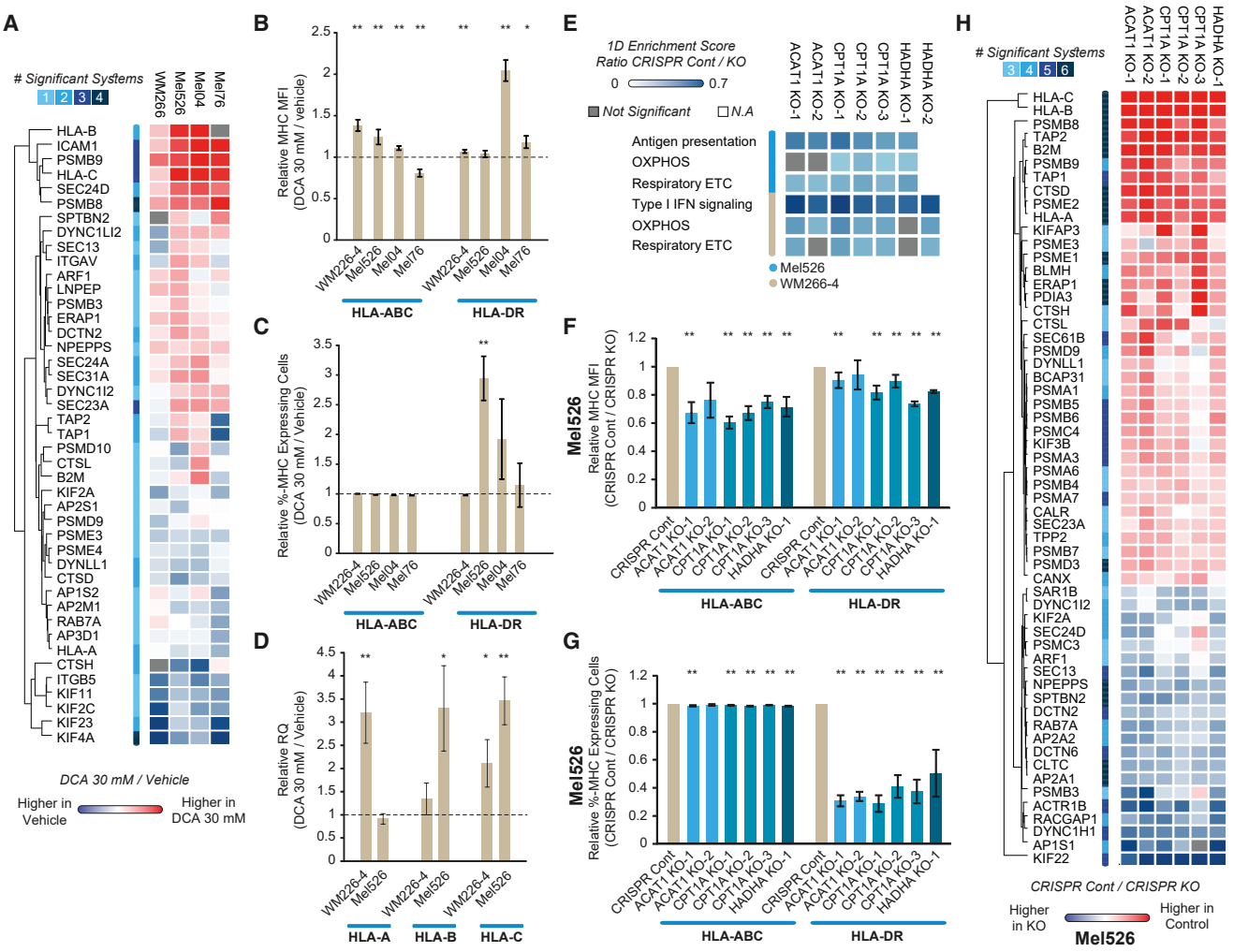

Figure 6. Metabolic Control of Antigen Presentation

(A) Proteomic profiles of all "antigen processing and presentation" (GOBP category) proteins that were significantly different upon DCA treatment in at least one cell line (FDR q value < 0.05, S0 = 0.1). Values are log2 LFQ intensity ratio of DCA-treated to vehicle. Color bar indicates the number of significant systems per protein. See also Table S5.

(B and C) Flow-cytometry analysis of the change in the HLA-ABC and HLA-DR signal (B) or percentage of stained cells (C) upon treatment with 30 mM DCA in four melanoma cell lines. Values are ratio of DCA-treated to vehicle control. Data are represented as mean ± SEM. *p < 0.05; **p < 0.1.

(D) RT-qPCR analysis of the RNA expression changes of HLA-A, HLA-B, and HLA-C upon treatment with 30 mM DCA. Values are ratio of DCA-treated to vehicle control. Data are represented as mean ± SEM. *p < 0.05; **p < 0.1.

(E) One-dimension annotation enrichment analysis shows antigen presentation or type I IFN signaling enrichment along with mitochondrial respiration enrichment in the CRISPR control cells (FDR q value < 0.02). See also Table S6A and S6B.

(F and G) Flow-cytometry measurement of the changes in HLA-ABC and HLA-DR signal (F) or percentage of stained Mel526 cells (G). Data are represented as mean ± SEM. *p < 0.05; **p < 0.1.

(H) Proteomic profiles of all antigen processing and presentation (GOBP category) proteins that were significantly different in at least three gene knockouts in Mel526. (FDR q value < 0.05, S0 = 0.1). Values are log2 LFQ intensity ratio of CRISPR control to CRISPR KO.

immunoproteasome subunits PSMB8 and PSMB9 and the aminopeptidase ERAP1 (Student's t test permutation-based FDR q value < 0.05, S0 = 0.1) (Figure 6A; Table S5). Among the MHC class I proteins, HLA-A expression was slightly decreased, whereas HLA-B and HLA-C were significantly increased in most melanoma cell lines upon DCA treatment, and the key antigen presentation players TAP1, TAP2, and B2M showed differential behavior in the different cell lines. Of note, several antigen presentation proteins were lower upon DCA treatment, mainly vesicle-mediated transport proteins, such as kinesin superfamily proteins (KIFs), cathepsins, and AP complex subunits; these affect mostly MHC class II compartment transport (Neefjes et al., 2011). In accordance with the proteomics results, we found that treatment with DCA increased HLA presentation on the cell surface and increased mRNA expression levels (Figures 6B–6D and S6A). We further examined whether inhibition of

mitochondrial function can elicit opposite response. We inhibited oxidative phosphorylation with rotenone, antimycin or oligomycin, inhibited beta-oxidation with etomoxir, or inhibited ACAT1 with avasimibe. OXPHOS inhibition decreased MHC class I presentation on the cell surface in three of the four cell lines. Specific inhibition of beta-oxidation and ACAT1 had milder effects but showed similar trends (Figures S6B–S6K). Altogether, these results suggest that the metabolic state is not only correlated with response to treatment, but also has a regulatory role in increasing overall antigen presentation, mainly MHC class I machinery. The use of metabolic inhibitors showed that, despite the emphasis on beta-oxidation, MHC presentation is affected by mitochondrial activity in general.

To directly associate between the signature proteins and antigen presentation, we used CRISPR-Cas9 system to knock out two TIL signature genes, *ACAT1* and *HADHA*, in WM266-4 and Mel526 melanoma cell lines. In addition, we knocked out the major regulator of fatty acid oxidation *CPT1A* in the same cells (Figures S7A–S7B). Proteomic analysis of the CRISPR KO cells showed significant enrichment of antigen presentation and IFN signaling along with OXPHOS and respiratory electron transport chain (ETC) processes in the control compared with KO cells (1D enrichment analysis, FDR q value < 0.02) (Figure 6E; Tables S6A–S6B). Analysis of oxygen consumption rate (OCR) showed variable effects. KO of *ACAT1* and *CPT1A* reduced maximal OCR and the spare respiratory capacity in WM266-4, and KO of *HADHA* and *CPT1A* slightly reduced the spare respiratory capacity in Mel526 (Figures S7C–S7H). Presumably, the differences in culture conditions in the OCR measurements, and potentially also compensatory effects in the clones, led to some variation in OCR changes. To further investigate mitochondrial function, we quantified mitochondrial mass, as measured by MitoTracker staining. Mitochondrial staining was increased in most KO systems in both cell lines (Figures S7I–S7J). We speculate that this increase partially compensates for the KO of these metabolic enzymes, leading to variable overall OCR. Integration of these results shows that oxygen consumption per mitochondria is reduced in most systems, and the variation between the clones is probably related to the *in vitro* growth conditions.

Investigation of the downstream effects of the genetic perturbations showed reduced MHC class I intensity and reduced percent of HLA class II presenting cells upon *ACAT1, HADHA*, or *CPT1A* knockout, primarily in Mel526 cells (Figures 6F, 6G, S8A, and S8B). Proteomic analysis further verified these results (Figures S8C and S8D) and showed higher control/KO ratios in other key antigen presentation machinery proteins, including immunoproteasome subunits PSMB8 and PSMB9, ERAP1, TAP1, TAP2, TAPBP, B2M, and PD1A3 (Student's t test, permutation-based FDR q value < 0.05, S0 = 0.5) (Figures 6H and S8E–S8G; Tables S6C–S6F). These results show that even a single mitochondrial protein from our TIL signature can affect antigen presentation machinery and MHC class I expression.

The metabolic effects on antigen presentation suggest that these might affect T cell recognition and tumor cell killing. To examine this hypothesis, we co-cultured the KO or control melanoma cells with matching T cells and monitored cell death by LDH secretion. In agreement with the decreased expression of antigen presentation machinery proteins, specific T cell killing was significantly reduced upon KO of *ACAT1*, *HADHA*, and *CPT1A* (Figure 7A). To examine these effects via *in vivo* mouse models, we knocked out *Acat1* in YUMMER1.7 (clone D4J) (Meeth et al., 2016; Wang et al., 2017b), a mouse melanoma cell line (Figure S8H), and monitored the effects on tumor growth and immune infiltration in immune-competent mice. Monitoring the tumors over 17 days showed that *Acat1* KO induces a marked increase in tumor growth (Figure 7B). On the basis of the reduced sensitivity to T cell killing observed *in vitro*, we hypothesized that *Acat1* KO reduces T cell recognition, and thereby promotes tumor progression. Indeed, *Acat1* KO tumor cells showed significantly reduced expression of MHC class I and PD1 ligand (*Pdl1*) at both the RNA and the protein levels (Figures 7C–7F and S8I–S8J), as well as *B2m* RNA levels (Figure S8K). Moreover, upon 24 h incubation with IFNG, the KO cells displayed lower induction of MHC class I, *Pdl1* and *B2m* (Figure 7G). Immune cell profiling showed lower levels of cytokine-producing T cells ($CD8^+TNFA^+IFNG^+$ and $CD4^+TNFA^+$) in the *Acat1*-KO tumors than in controls (Figures 7H and 7I), whereas the overall percentage of infiltrating $CD4^+$ and $CD8^+$ T cells did not vary (Figures 7I–7L). Of note, no difference in $IFNG^+$ single-producing $CD8^+$ T cells was observed, indicating that *Acat1* deficiency more prominently affected the number of polyfunctional $CD8^+$ T cells in melanoma. Furthermore, the fraction of monocytic myeloid cells ($CD45^+CD11B^+F4/80^{low}LY6C^{high}$) was significantly lower in the *Acat1*-KO tumors than in the control (Figure 7M), while the proportion of macrophages ($CD45^+CD11B^+F4/80^{high}LY6C^{low}$) was significantly higher (Figure 7N). $CD45^+$ $CD11B^+$ $F4/80^{low}$ $LY6C^{high}$ cells were previously associated with more inflamed tumors and improved overall survival (Perry et al., 2018). Overall these results show the importance of these proteins as regulators that affect the melanoma and immune cells both *in vitro* and *in vivo*.

DISCUSSION

Melanoma is an extensively studied cancer predominantly from an immunotherapeutic perspective. Transcriptomic analyses have enabled further examination of potential biomarkers to predict response (Hugo et al., 2016; Lauss et al., 2017; Riaz et al., 2017; Van Allen et al., 2015). We hypothesized that analysis at the proteomic level would unravel novel aspects of response not yet observed on the mRNA level. We present the proteomic landscape of 116 melanoma samples of patients treated by either TIL-based immunotherapy or PD1 blockade. Primarily, our dataset might serve the scientific community as a resource of clinical proteomic data, which is still sparse, especially in melanoma.

Our major findings link melanoma metabolism to immunogenicity and the response to two different modes of immunotherapy. Higher amounts of MHC molecules is directly associated with response to T cell killing (Sade-Feldman et al., 2017; Seliger, 2014); indeed, our immunohistochemistry (IHC) analyses show a correlation between metabolic protein expression and T cell activation, hence the oxidative metabolic state might render the tumor more "hot". We further observed lower MHC amounts and subsequently reduced T cell killing upon

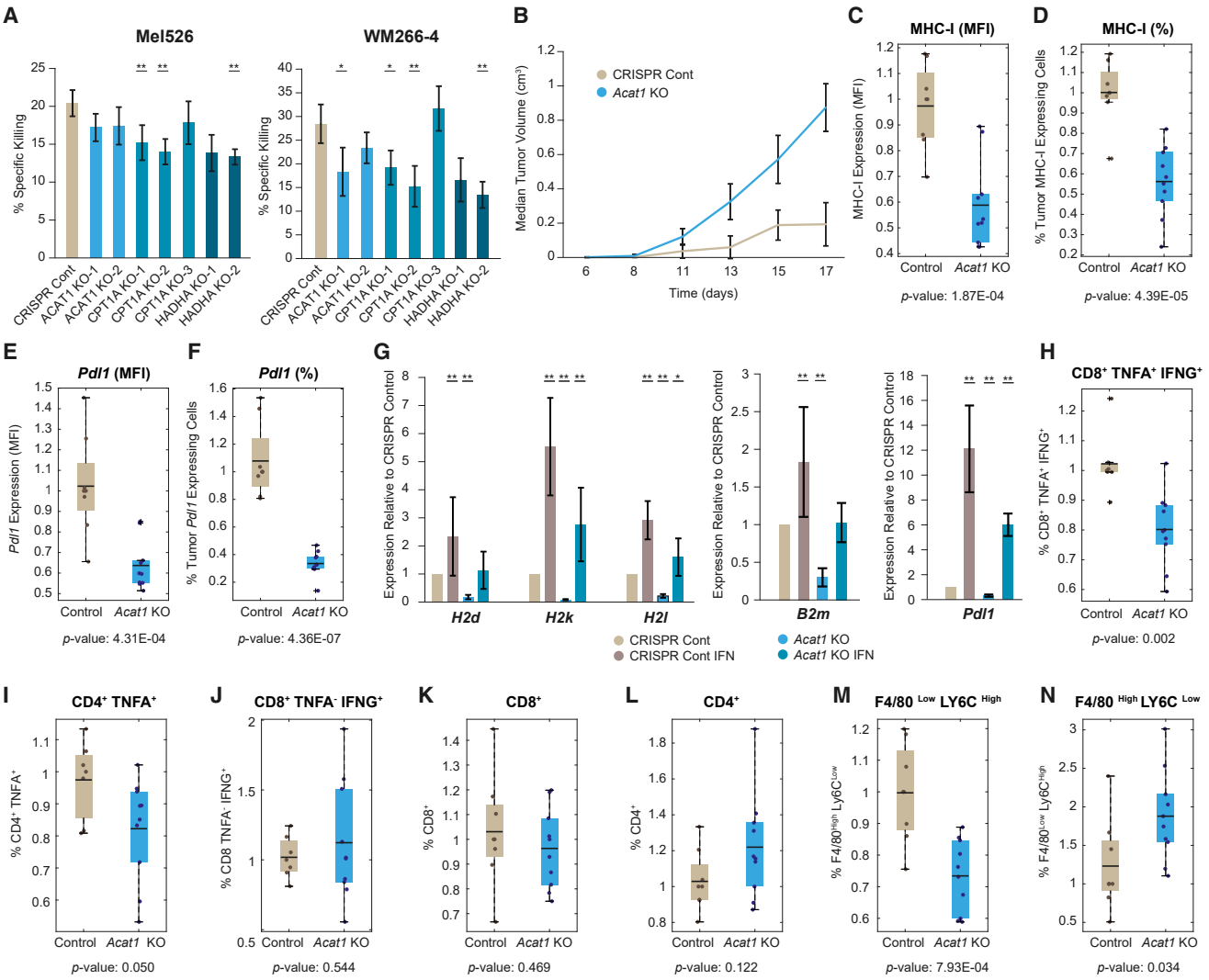

Figure 7. CRISPR KO Effects on Tumor Immunogenicity and T Cell Activity

(A) CRISPR-Cas9 knockout of *ACAT1*, *HADHA*, and *CPT1A* in WM266-4 (right) and Mel526 (left) cells reduces specific killing by T cells. KO cells were co-cultured with matched T cells and cell death was quantified based on LDH secretion. Data are represented as mean ± SEM. *p < 0.05; **p < 0.1.

(B–N) KO of *Acat1* was performed in YUMMER1.7 (clone D4J) mouse cells that were then injected into mice (control n = 8; *Acat1* KO n = 10). See also Figure S8H. *Acat1* KO cells presented enhanced tumor growth compared with control. Data are represented as mean ± SEM (B).

(C–F) Control and KO cells were analyzed by flow cytometry to determine MHC class I MFI (C); percentage of tumor-cell-presenting MHC class I (D); *Pdl1* MFI (E); and percentage of tumor-cell-presenting *Pdl1* (F).

(G) CRISPR Control and KO cells were either treated with IFNG (10 ng) or not and examined for IFN-induced mRNA expression of the indicated genes. *p < 0.05; **p < 0.1.

(H–N) Flow-cytometry-based profiling of immune cell population. Shown is the percentage of $CD45^+CD11b^-CD8^+TNFA^+IFNG^+$-expressing cells (H); percentage of $CD45^+CD11b^-CD4^+TNFA^+$-expressing cells (I); percentage of $CD45^+CD11b^-CD8^+TNFA^-IFNG^+$-expressing cells (J); percentage of $CD45^+CD11b^-CD8^+$-expressing cells (K); percentage of $CD45^+CD11b^-CD4^+$-expressing cells (L); percentage of $CD45^+CD11b^+F4/80^{low}LY6C^{high}$-expressing cells (M); and percentage of $CD45^+CD11b^+F4/80^{high}LY6C^{low}$-expressing cells (N).

All values are relative to untreated CRISPR control cells. Gene expression was normalized relative to actin. Data are represented as mean ± SEM.

ACAT1, HADHA, or *CPT1A* knockout. Elevation in MHC class I molecules coincided with MHC class II elevation, in agreement with the established role of $CD4^+$ T cells in immunotherapy (Hunder et al., 2008; Johnson et al., 2016; Kreiter et al., 2015; Tran et al., 2014). Importantly, the effect of melanoma metabolism on antigen presentation was not limited to the expression of MHC molecules but included multiple key members of the antigen processing and presentation machinery. Montoya and colleague have pointed out that antigen processing and binding to the MHC molecules are major limiting steps for antigen presentation, along with the availability and avidity of the MHC molecules (Montoya and Del Val, 1999), indicating the importance of upregulating other key members in this machinery in order for the higher MHC amounts to affect immunogenicity.

Metabolic regulation affected both protein and mRNA levels of MHC, which indicates there might be a metabolic-transcriptional link. Two potential mediators of the signal are NLRC5, a well-established transcriptional regulator of MHC class I (Jongsma et al., 2017; Meissner et al., 2010), and STAT1 (Zhou, 2009), which was significantly higher in our clinical data in the responder tumors than in the non-responders, along with enrichment of interferon regulatory factor 1 (IRF1) targets. STAT1 was previously shown to regulate mitochondrial activity, (Pitroda et al., 2009; Sisler et al., 2015), but its regulation by the mitochondria is still unknown. (Ahmed and Cassol, 2017; Mills et al., 2016; York et al., 2015). Beyond these transcriptional regulators, two additional mechanisms previously linked metabolism to MHC. Charni et al. showed that elevated OXPHOS increases MHC class I presentation by activating extracellular signal-regulated kinase 5 (ERK5) (Charni et al., 2009; Charni et al., 2010). Hypoxia-inducible factor-1α (HIF-1α), a master regulator of glycolysis, was recently shown to downregulate MHC class I and TAP proteins in sarcoma mouse models (Sethumadhavan et al., 2017). Further research is needed to decipher which of these mediates the metabolism-transcription link in our systems and potentially identify the broader regulatory mechanism.

Beyond the melanoma-intrinsic effects on antigen presentation, altered tumor immunogenicity can also result from changes in the metabolic interactions within the tumor microenvironment. In recent years, there has been much focus on the association between metabolism and immune response, primarily focusing on T cells (Buck et al., 2017; Ho and Kaech, 2017; Lim et al., 2017; Pearce et al., 2013) and immune checkpoints (Patsoukis et al., 2015). Metabolic cross-talk can also involve the inhibitory effects of extracellular lactate on $CD8^+$ T cells (Brand et al., 2016; Cascone et al., 2018). Cancer cells in the responder samples, in accordance with their elevated mitochondrial activity, might have lower lactate secretion, leading to lower inhibitory effects on the T cells in the microenvironment. Higher mitochondrial activity might also render cells more susceptible to granzyme-B-mediated mitochondrial apoptosis induced by T cells, and higher ATP production by OXPHOS might serve the large energetic demand of the entire process of antigen presentation. In addition to these potential mechanisms, recent studies showed that highly glycolytic tumors restrict glucose and phosphoenolpyruvate (PEP) in the tumor microenvironment, thereby inhibiting T cells by disrupting Ca^{2+}-NFAT signaling (Ho et al., 2015), and reducing their glycolytic capacity and IFNG production (Chang et al., 2015), leading to resistance to immunotherapy (Cascone et al., 2018). In our data, the responder tumors are enriched with glycolysis or gluconeogenesis related proteins; however, the enrichment of multiple mitochondrial pathways involving fatty acid oxidation, ketone body metabolism, TCA cycle, and OXPHOS, as well as their interconnectivity, suggest that glycolysis is part of a larger metabolic flux toward oxidative respiration, thus relying less on glucose. Accordingly, we speculate that the higher tumor mitochondrial activity might consume less glucose compared with non-responders, thereby reducing the competition with the cytotoxic T lymphocytes (CTLs). Of note, recent reports indicate that the same type of immune cells can act differently upon changes in the microenvironment. Specifically, although effector T cells are by and large glycolytic, under hypoxic or hypoglycemic tumor conditions T cells that rely on fatty acid oxidation are more cytotoxic than those that do not (Scharping et al., 2016; Zhang et al., 2017). Moreover, different immune cells are affected differently upon metabolic changes in the tumor microenvironment. For instance, although lipid uptake by dendritic cells renders them less functional (Herber et al., 2010), tissue-resident memory T cells require lipid uptake for longer survival (Pan et al., 2017). Our *in vivo* results already show that the metabolic change in the melanoma affects multiple cell types or states, and further functional research will uncover the intricate relationships between the distinct cell populations upon high mitochondrial activity.

Altogether, we propose that the metabolic state of melanoma cells dictates cellular changes that affects vulnerability to T cell killing through both intrinsic changes in the antigen presentation machinery and extrinsic alterations of the tumor microenvironment. These results add an additional layer to the complex immune-metabolic network, which might have important therapeutic implications.

STAR★METHODS

Detailed methods are provided in the online version of this paper and include the following:

- KEY RESOURCES TABLE
- LEAD CONTACT AND MATERIALS AVAILABILITY
- EXPERIMENTAL MODEL AND SUBJECT DETAILS
  - Tumor sample collection
  - Cell lines
- METHOD DETAILS
  - Proteomics sample preparation
  - LC-MS-based proteomics
  - Immunohistochemistry (IHC) staining
  - CRISPR-Cas9 gene knockout
  - T cell killing assay
  - Tumor growth assessment and tumor digestion
  - Flow cytometry analysis
  - RNA expression analysis of MHC class I
  - MitoTracker staining and imaging
  - Seahorse measurements
- QUANTIFICATION AND STATISTICAL ANALYSIS
  - Proteomics raw MS data processing
  - Proteomics statistical analysis
  - RNA -sequencing data analysis
- DATA AND CODE AVAILABILITY
  - Data resources

SUPPLEMENTAL INFORMATION

Supplemental Information can be found online at https://doi.org/10.1016/j.cell.2019.08.012.

ACKNOWLEDGMENTS

We thank Prof. Juergen Cox, Dr. Livnat Jerby-Arnon, and Dr. Yael Elbaz-Alon for fruitful discussions and Dr. Keren Yizhak for her assistance in computational analyses. We thank Diana Nemichenitzer for technical assistance in sample preparation. We thank the Lemelbaum family for the generous

continuous support. This work was funded by the Melanoma Research Alliance Saban Family Team Science Award and Kamin grant of the Israel Innovation Authority to G.M. and T.G., Samueli Foundation Grant for Integrative Immuno-Oncology to G.M., NIH R01 CA216102 to G.S.S. and S.M.K., the Salkexcellerators Postdoctoral fellowship to K.C.M., and NOMIS Center Postdoctoral Foundation and the National Cancer Center to S.K.V.

AUTHOR CONTRIBUTION

Conceptualization, T.G., G.M., and M.H.; Investigation, M.H., R.O., S.K.V., K.C.M., M.M., V.C., R.A., S.X., G.Y.A., and G.D.B.; Formal analysis, M.H., M.M., and E.N.B; Validation, M.M. and E.N.B.; Resources, I.B., E.M., E.N.B., E.G., S.A., L.A., M.J.B., and J.S.; Methodology, M.B., M.A., A.S., and N.K.; Data curation, M.H. and E.M.; Writing-Original draft, M.H., T.G., and G.M.; Writing-Review and editing, M.H., T.G., G.M., S.M.K., and G.S.S.; Visualization, M.H.; Supervision, T.G., G.M., S.M.K., and G.S.S.; Funding Acquisition, T.G., G.M., G.S.S., S.M.K., K.C.M., and S.K.V.

DECLARATION OF INTERESTS

A provisional patent application has been filed.

Received: March 22, 2019
Revised: June 24, 2019
Accepted: August 6, 2019
Published: September 5, 2019

REFERENCES

Ahmed, D., and Cassol, E. (2017). Role of cellular metabolism in regulating type I interferon responses: Implications for tumour immunology and treatment. Cancer Lett. *409*, 20–29.

Ardiani, A., Gameiro, S.R., Palena, C., Hamilton, D.H., Kwilas, A., King, T.H., Schlom, J., and Hodge, J.W. (2014). Vaccine-mediated immunotherapy directed against a transcription factor driving the metastatic process. Cancer Res. *74*, 1945–1957.

Auslander, N., Zhang, G., Lee, J.S., Frederick, D.T., Miao, B., Moll, T., Tian, T., Wei, Z., Madan, S., Sullivan, R.J., et al. (2018). Robust prediction of response to immune checkpoint blockade therapy in metastatic melanoma. Nat. Med. *24*, 1545–1549.

Ayers, M., Lunceford, J., Nebozhyn, M., Murphy, E., Loboda, A., Kaufman, D.R., Albright, A., Cheng, J.D., Kang, S.P., Shankaran, V., et al. (2017). IFN-γ-related mRNA profile predicts clinical response to PD-1 blockade. J. Clin. Invest. *127*, 2930–2940.

Besser, M.J., Shapira-Frommer, R., Treves, A.J., Zippel, D., Itzhaki, O., Hershkovitz, L., Levy, D., Kubi, A., Hovav, E., Chermoshniuk, N., et al. (2010). Clinical responses in a phase II study using adoptive transfer of short-term cultured tumor infiltration lymphocytes in metastatic melanoma patients. Clin. Cancer Res. *16*, 2646–2655.

Besser, M.J., Shapira-Frommer, R., Itzhaki, O., Treves, A.J., Zippel, D.B., Levy, D., Kubi, A., Shoshani, N., Zikich, D., Ohayon, Y., et al. (2013). Adoptive transfer of tumor-infiltrating lymphocytes in patients with metastatic melanoma: intent-to-treat analysis and efficacy after failure to prior immunotherapies. Clin. Cancer Res. *19*, 4792–4800.

Brand, A., Singer, K., Koehl, G.E., Kolitzus, M., Schoenhammer, G., Thiel, A., Matos, C., Bruss, C., Klobuch, S., Peter, K., et al. (2016). LDHA-associated lactic acid production blunts tumor immunosurveillance by T and NK cells. Cell Metab. *24*, 657–671.

Buck, M.D., Sowell, R.T., Kaech, S.M., and Pearce, E.L. (2017). Metabolic instruction of immunity. Cell *169*, 570–586.

Cancer Genome Atlas Network (2015). Genomic classification of cutaneous melanoma. Cell *161*, 1681–1696.

Cascone, T., McKenzie, J.A., Mbofung, R.M., Punt, S., Wang, Z., Xu, C., Williams, L.J., Wang, Z., Bristow, C.A., Carugo, A., et al. (2018). Increased tumor glycolysis characterizes immune resistance to adoptive T cell therapy. Cell Metab *27*, 977–987.

Chang, C.H., Qiu, J., O'Sullivan, D., Buck, M.D., Noguchi, T., Curtis, J.D., Chen, Q., Gindin, M., Gubin, M.M., van der Windt, G.J., et al. (2015). Metabolic competition in the tumor microenvironment is a driver of cancer progression. Cell *162*, 1229–1241.

Charni, S., Aguilo, J.I., Garaude, J., de Bettignies, G., Jacquet, C., Hipskind, R.A., Singer, D., Anel, A., and Villalba, M. (2009). ERK5 knockdown generates mouse leukemia cells with low MHC class I levels that activate NK cells and block tumorigenesis. J. Immunol. *182*, 3398–3405.

Charni, S., de Bettignies, G., Rathore, M.G., Aguiló, J.I., van den Elsen, P.J., Haouzi, D., Hipskind, R.A., Enriquez, J.A., Sanchez-Beato, M., Pardo, J., et al. (2010). Oxidative phosphorylation induces de novo expression of the MHC class I in tumor cells through the ERK5 pathway. J. Immunol. *185*, 3498–3503.

Conforti, F., Pala, L., Bagnardi, V., De Pas, T., Martinetti, M., Viale, G., Gelber, R.D., and Goldhirsch, A. (2018). Cancer immunotherapy efficacy and patients' sex: a systematic review and meta-analysis. Lancet Oncol. *19*, 737–746.

Cox, J., and Mann, M. (2008). MaxQuant enables high peptide identification rates, individualized p.p.b.-range mass accuracies and proteome-wide protein quantification. Nat. Biotechnol. *26*, 1367–1372.

Cox, J., and Mann, M. (2012). 1D and 2D annotation enrichment: a statistical method integrating quantitative proteomics with complementary high-throughput data. BMC Bioinformatics *13* (*Suppl 16*), S12.

Cox, J., Neuhauser, N., Michalski, A., Scheltema, R.A., Olsen, J.V., and Mann, M. (2011). Andromeda: a peptide search engine integrated into the MaxQuant environment. J. Proteome Res. *10*, 1794–1805.

Dudley, M.E., Wunderlich, J.R., Yang, J.C., Sherry, R.M., Topalian, S.L., Restifo, N.P., Royal, R.E., Kammula, U., White, D.E., Mavroukakis, S.A., et al. (2005). Adoptive cell transfer therapy following non-myeloablative but lymphodepleting chemotherapy for the treatment of patients with refractory metastatic melanoma. J. Clin. Oncol. *23*, 2346–2357.

Geiger, T., Cox, J., Ostasiewicz, P., Wisniewski, J.R., and Mann, M. (2010). Super-SILAC mix for quantitative proteomics of human tumor tissue. Nat. Methods *7*, 383–385.

Gibney, G.T., Weiner, L.M., and Atkins, M.B. (2016). Predictive biomarkers for checkpoint inhibitor-based immunotherapy. Lancet Oncol. *17*, e542–e551.

Goto, Y., Koyanagi, K., Narita, N., Kawakami, Y., Takata, M., Uchiyama, A., Nguyen, L., Nguyen, T., Ye, X., Morton, D.L., and Hoon, D.S. (2010). Aberrant fatty acid-binding protein-7 gene expression in cutaneous malignant melanoma. J. Invest. Dermatol. *130*, 221–229.

Herber, D.L., Cao, W., Nefedova, Y., Novitskiy, S.V., Nagaraj, S., Tyurin, V.A., Corzo, A., Cho, H.I., Celis, E., Lennox, B., et al. (2010). Lipid accumulation and dendritic cell dysfunction in cancer. Nat. Med. *16*, 880–886.

Ho, P.C., and Kaech, S.M. (2017). Reenergizing T cell anti-tumor immunity by harnessing immunometabolic checkpoints and machineries. Curr. Opin. Immunol. *46*, 38–44.

Ho, P.C., Bihuniak, J.D., Macintyre, A.N., Staron, M., Liu, X., Amezquita, R., Tsui, Y.C., Cui, G., Micevic, G., Perales, J.C., et al. (2015). Phosphoenolpyruvate is a metabolic checkpoint of anti-tumor T cell responses. Cell *162*, 1217–1228.

Hodi, F.S., O'Day, S.J., McDermott, D.F., Weber, R.W., Sosman, J.A., Haanen, J.B., Gonzalez, R., Robert, C., Schadendorf, D., Hassel, J.C., et al. (2010). Improved survival with ipilimumab in patients with metastatic melanoma. N. Engl. J. Med. *363*, 711–723.

Hugo, W., Zaretsky, J.M., Sun, L., Song, C., Moreno, B.H., Hu-Lieskovan, S., Berent-Maoz, B., Pang, J., Chmielowski, B., Cherry, G., et al. (2016). Genomic and transcriptomic features of response to anti-PD-1 therapy in metastatic melanoma. Cell *165*, 35–44.

Hunder, N.N., Wallen, H., Cao, J., Hendricks, D.W., Reilly, J.Z., Rodmyre, R., Jungbluth, A., Gnjatic, S., Thompson, J.A., and Yee, C. (2008). Treatment of metastatic melanoma with autologous CD4+ T cells against NY-ESO-1. N. Engl. J. Med. *358*, 2698–2703.

Jerby-Arnon, L., Shah, P., Cuoco, M.S., Rodman, C., Su, M.J., Melms, J.C., Leeson, R., Kanodia, A., Mei, S., Lin, J.R., et al. (2018). A cancer cell program promotes T cell exclusion and resistance to checkpoint blockade. Cell *175*, 984–997.

Johnson, D.B., Estrada, M.V., Salgado, R., Sanchez, V., Doxie, D.B., Opalenik, S.R., Vilgelm, A.E., Feld, E., Johnson, A.S., Greenplate, A.R., et al. (2016). Melanoma-specific MHC-II expression represents a tumour-autonomous phenotype and predicts response to anti-PD-1/PD-L1 therapy. Nat. Commun. *7*, 10582.

Jongsma, M.L.M., Guarda, G., and Spaapen, R.M. (2017). The regulatory network behind MHC class I expression. Mol. Immunol. *17*, 30598–30599.

Kreiter, S., Vormehr, M., van de Roemer, N., Diken, M., Löwer, M., Diekmann, J., Boegel, S., Schrörs, B., Vascotto, F., Castle, J.C., et al. (2015). Mutant MHC class II epitopes drive therapeutic immune responses to cancer. Nature *520*, 692–696.

Lauss, M., Donia, M., Harbst, K., Andersen, R., Mitra, S., Rosengren, F., Salim, M., Vallon-Christersson, J., Törngren, T., Kvist, A., et al. (2017). Mutational and putative neoantigen load predict clinical benefit of adoptive T cell therapy in melanoma. Nat. Commun. *8*, 1738.

Li, H., van der Leun, A.M., Yofe, I., Lubling, Y., Gelbard-Solodkin, D., van Akkooi, A.C.J., van den Braber, M., Rozeman, E.A., Haanen, J., Blank, C.U., et al. (2018). Dysfunctional CD8 T cells form a proliferative, dynamically regulated compartment within human melanoma. Cell *176*, 775–789.

Liebermeister, W., Noor, E., Flamholz, A., Davidi, D., Bernhardt, J., and Milo, R. (2014). Visual account of protein investment in cellular functions. Proc. Natl. Acad. Sci. USA *111*, 8488–8493.

Lim, S., Phillips, J.B., Madeira da Silva, L., Zhou, M., Fodstad, O., Owen, L.B., and Tan, M. (2017). Interplay between immune checkpoint proteins and cellular metabolism. Cancer Res. *77*, 1245–1249.

Manguso, R.T., Pope, H.W., Zimmer, M.D., Brown, F.D., Yates, K.B., Miller, B.C., Collins, N.B., Bi, K., LaFleur, M.W., Juneja, V.R., et al. (2017). In vivo CRISPR screening identifies Ptpn2 as a cancer immunotherapy target. Nature *547*, 413–418.

Meeth, K., Wang, J.X., Micevic, G., Damsky, W., and Bosenberg, M.W. (2016). The YUMM lines: a series of congenic mouse melanoma cell lines with defined genetic alterations. Pigment Cell Melanoma Res. *29*, 590–597.

Meissner, T.B., Li, A., Biswas, A., Lee, K.H., Liu, Y.J., Bayir, E., Iliopoulos, D., van den Elsen, P.J., and Kobayashi, K.S. (2010). NLR family member NLRC5 is a transcriptional regulator of MHC class I genes. Proc. Natl. Acad. Sci. USA *107*, 13794–13799.

Mertins, P., Mani, D.R., Ruggles, K.V., Gillette, M.A., Clauser, K.R., Wang, P., Wang, X., Qiao, J.W., Cao, S., Petralia, F., et al.; NCI CPTAC (2016). Proteogenomics connects somatic mutations to signalling in breast cancer. Nature *534*, 55–62.

Mills, E.L., Kelly, B., Logan, A., Costa, A.S.H., Varma, M., Bryant, C.E., Tourlomousis, P., Dabritz, J.H.M., Gottlieb, E., Latorre, I., et al. (2016). Succinate dehydrogenase supports metabolic repurposing of mitochondria to drive inflammatory macrophages. Cell *167*, 457–470.

Montoya, M., and Del Val, M. (1999). Intracellular rate-limiting steps in MHC class I antigen processing. J. Immunol. *163*, 1914–1922.

Neefjes, J., Jongsma, M.L., Paul, P., and Bakke, O. (2011). Towards a systems understanding of MHC class I and MHC class II antigen presentation. Nat. Rev. Immunol. *11*, 823–836.

Pan, Y., Tian, T., Park, C.O., Lofftus, S.Y., Mei, S., Liu, X., Luo, C., O'Malley, J.T., Gehad, A., Teague, J.E., et al. (2017). Survival of tissue-resident memory T cells requires exogenous lipid uptake and metabolism. Nature *543*, 252–256.

Patsoukis, N., Bardhan, K., Chatterjee, P., Sari, D., Liu, B., Bell, L.N., Karoly, E.D., Freeman, G.J., Petkova, V., Seth, P., et al. (2015). PD-1 alters T-cell metabolic reprogramming by inhibiting glycolysis and promoting lipolysis and fatty acid oxidation. Nat. Commun. *6*, 6692.

Pearce, E.L., Poffenberger, M.C., Chang, C.H., and Jones, R.G. (2013). Fueling immunity: insights into metabolism and lymphocyte function. Science *342*, 1242454.

Perry, C.J., Muñoz-Rojas, A.R., Meeth, K.M., Kellman, L.N., Amezquita, R.A., Thakral, D., Du, V.Y., Wang, J.X., Damsky, W., Kuhlmann, A.L., et al. (2018). Myeloid-targeted immunotherapies act in synergy to induce inflammation and antitumor immunity. J. Exp. Med. *215*, 877–893.

Pitroda, S.P., Wakim, B.T., Sood, R.F., Beveridge, M.G., Beckett, M.A., MacDermed, D.M., Weichselbaum, R.R., and Khodarev, N.N. (2009). STAT1-dependent expression of energy metabolic pathways links tumour growth and radioresistance to the Warburg effect. BMC Med. *7*, 68.

Pitt, J.M., Vétizou, M., Daillère, R., Roberti, M.P., Yamazaki, T., Routy, B., Lepage, P., Boneca, I.G., Chamaillard, M., Kroemer, G., and Zitvogel, L. (2016). Resistance mechanisms to immune-checkpoint blockade in cancer: tumor-intrinsic and -extrinsic factors. Immunity *44*, 1255–1269.

Radvanyi, L.G., Bernatchez, C., Zhang, M., Fox, P.S., Miller, P., Chacon, J., Wu, R., Lizee, G., Mahoney, S., Alvarado, G., et al. (2012). Specific lymphocyte subsets predict response to adoptive cell therapy using expanded autologous tumor-infiltrating lymphocytes in metastatic melanoma patients. Clin. Cancer Res. *18*, 6758–6770.

Ran, F.A., Hsu, P.D., Wright, J., Agarwala, V., Scott, D.A., and Zhang, F. (2013). Genome engineering using the CRISPR-Cas9 system. Nat. Protoc. *8*, 2281–2308.

Rappsilber, J., Ishihama, Y., and Mann, M. (2003). Stop and go extraction tips for matrix-assisted laser desorption/ionization, nanoelectrospray, and LC/MS sample pretreatment in proteomics. Anal. Chem. *75*, 663–670.

Riaz, N., Havel, J.J., Makarov, V., Desrichard, A., Urba, W.J., Sims, J.S., Hodi, F.S., Martin-Algarra, S., Mandal, R., Sharfman, W.H., et al. (2017). Tumor and microenvironment evolution during immunotherapy with nivolumab. Cell *171*, 934–949.

Robert, C., Thomas, L., Bondarenko, I., O'Day, S., Weber, J., Garbe, C., Lebbe, C., Baurain, J.F., Testori, A., Grob, J.J., et al. (2011). Ipilimumab plus dacarbazine for previously untreated metastatic melanoma. N. Engl. J. Med. *364*, 2517–2526.

Rosenberg, S.A., Packard, B.S., Aebersold, P.M., Solomon, D., Topalian, S.L., Toy, S.T., Simon, P., Lotze, M.T., Yang, J.C., Seipp, C.A., et al. (1988). Use of tumor-infiltrating lymphocytes and interleukin-2 in the immunotherapy of patients with metastatic melanoma. A preliminary report. N. Engl. J. Med. *319*, 1676–1680.

Rudolph, J.D., and Cox, J. (2019). A Network module for the perseus software for computational proteomics facilitates proteome interaction graph analysis. J. Proteome Res. *18*, 2052–2064.

Sade-Feldman, M., Jiao, Y.J., Chen, J.H., Rooney, M.S., Barzily-Rokni, M., Eliane, J.P., Bjorgaard, S.L., Hammond, M.R., Vitzthum, H., Blackmon, S.M., et al. (2017). Resistance to checkpoint blockade therapy through inactivation of antigen presentation. Nat. Commun. *8*, 1136.

Sanjana, N.E., Shalem, O., and Zhang, F. (2014). Improved vectors and genome-wide libraries for CRISPR screening. Nat. Methods *11*, 783–784.

Schadendorf, D., Hodi, F.S., Robert, C., Weber, J.S., Margolin, K., Hamid, O., Patt, D., Chen, T.T., Berman, D.M., and Wolchok, J.D. (2015). Pooled analysis of long-term survival data from phase II and phase III trials of ipilimumab in unresectable or metastatic melanoma. J. Clin. Oncol. *33*, 1889–1894.

Scharping, N.E., Menk, A.V., Moreci, R.S., Whetstone, R.D., Dadey, R.E., Watkins, S.C., Ferris, R.L., and Delgoffe, G.M. (2016). The tumor microenvironment represses T cell mitochondrial biogenesis to drive intratumoral T cell metabolic insufficiency and dysfunction. Immunity *45*, 374–388.

Scheltema, R.A., Hauschild, J.P., Lange, O., Hornburg, D., Denisov, E., Damoc, E., Kuehn, A., Makarov, A., and Mann, M. (2014). The Q Exactive HF, a Benchtop mass spectrometer with a pre-filter, high-performance quadrupole and an ultra-high-field Orbitrap analyzer. Mol. Cell. Proteomics *13*, 3698–3708.

Seliger, B. (2014). The link between MHC class I abnormalities of tumors, oncogenes, tumor suppressor genes, and transcription factors. J. Immunotoxicol. *11*, 308–310.

Sethumadhavan, S., Silva, M., Philbrook, P., Nguyen, T., Hatfield, S.M., Ohta, A., and Sitkovsky, M.V. (2017). Hypoxia and hypoxia-inducible factor (HIF)

downregulate antigen-presenting MHC class I molecules limiting tumor cell recognition by T cells. PLoS ONE *12*, e0187314.

Shannon, P., Markiel, A., Ozier, O., Baliga, N.S., Wang, J.T., Ramage, D., Amin, N., Schwikowski, B., and Ideker, T. (2003). Cytoscape: a software environment for integrated models of biomolecular interaction networks. Genome Res. *13*, 2498–2504.

Singer, M., Wang, C., Cong, L., Marjanovic, N.D., Kowalczyk, M.S., Zhang, H., Nyman, J., Sakuishi, K., Kurtulus, S., Gennert, D., et al. (2016). A distinct gene module for dysfunction uncoupled from activation in tumor-infiltrating T cells. Cell *166*, 1500–1511.

Sisler, J.D., Morgan, M., Raje, V., Grande, R.C., Derecka, M., Meier, J., Cantwell, M., Szczepanek, K., Korzun, W.J., Lesnefsky, E.J., et al. (2015). The signal transducer and activator of transcription 1 (stat1) inhibits mitochondrial biogenesis in liver and fatty acid oxidation in adipocytes. PLoS ONE *10*, e0144444.

Sumimoto, H., Imabayashi, F., Iwata, T., and Kawakami, Y. (2006). The BRAF-MAPK signaling pathway is essential for cancer-immune evasion in human melanoma cells. J. Exp. Med. *203*, 1651–1656.

Szklarczyk, D., Morris, J.H., Cook, H., Kuhn, M., Wyder, S., Simonovic, M., Santos, A., Doncheva, N.T., Roth, A., Bork, P., et al. (2017). The STRING database in 2017: quality-controlled protein-protein association networks, made broadly accessible. Nucleic Acids Res. *45* (D1), D362–D368.

Tirosh, I., Izar, B., Prakadan, S.M., Wadsworth, M.H., 2nd, Treacy, D., Trombetta, J.J., Rotem, A., Rodman, C., Lian, C., Murphy, G., et al. (2016). Dissecting the multicellular ecosystem of metastatic melanoma by single-cell RNA-seq. Science *352*, 189–196.

Topalian, S.L., Hodi, F.S., Brahmer, J.R., Gettinger, S.N., Smith, D.C., McDermott, D.F., Powderly, J.D., Carvajal, R.D., Sosman, J.A., Atkins, M.B., et al. (2012). Safety, activity, and immune correlates of anti-PD-1 antibody in cancer. N. Engl. J. Med. *366*, 2443–2454.

Tran, E., Turcotte, S., Gros, A., Robbins, P.F., Lu, Y.C., Dudley, M.E., Wunderlich, J.R., Somerville, R.P., Hogan, K., Hinrichs, C.S., et al. (2014). Cancer immunotherapy based on mutation-specific CD4+ T cells in a patient with epithelial cancer. Science *344*, 641–645.

Tusher, V.G., Tibshirani, R., and Chu, G. (2001). Significance analysis of microarrays applied to the ionizing radiation response. Proc. Natl. Acad. Sci. USA *98*, 5116–5121.

Tyanova, S., Temu, T., Sinitcyn, P., Carlson, A., Hein, M.Y., Geiger, T., Mann, M., and Cox, J. (2016). The Perseus computational platform for comprehensive analysis of (prote)omics data. Nat. Methods *13*, 731–740.

Van Allen, E.M., Miao, D., Schilling, B., Shukla, S.A., Blank, C., Zimmer, L., Sucker, A., Hillen, U., Foppen, M.H.G., Goldinger, S.M., et al. (2015). Genomic correlates of response to CTLA-4 blockade in metastatic melanoma. Science *350*, 207–211.

Vogel, C., Abreu, Rde.S., Ko, D., Le, S.Y., Shapiro, B.A., Burns, S.C., Sandhu, D., Boutz, D.R., Marcotte, E.M., and Penalva, L.O. (2010). Sequence signatures and mRNA concentration can explain two-thirds of protein abundance variation in a human cell line. Mol. Syst. Biol. *6*, 400.

Wang, J., Ma, Z., Carr, S.A., Mertins, P., Zhang, H., Zhang, Z., Chan, D.W., Ellis, M.J., Townsend, R.R., Smith, R.D., et al. (2017a). Proteome profiling outperforms transcriptome profiling for coexpression based gene function prediction. Mol. Cell. Proteomics *16*, 121–134.

Wang, J., Perry, C.J., Meeth, K., Thakral, D., Damsky, W., Micevic, G., Kaech, S., Blenman, K., and Bosenberg, M. (2017b). UV-induced somatic mutations elicit a functional T cell response in the YUMMER1.7 mouse melanoma model. Pigment Cell Melanoma Res. *30*, 428–435.

Weide, B., Martens, A., Hassel, J.C., Berking, C., Postow, M.A., Bisschop, K., Simeone, E., Mangana, J., Schilling, B., Di Giacomo, A.M., et al. (2016). Baseline biomarkers for outcome of melanoma patients treated with pembrolizumab. Clin. Cancer Res. *22*, 5487–5496.

Wellenstein, M.D., and de Visser, K.E. (2018). Cancer-cell-intrinsic mechanisms shaping the tumor immune landscape. Immunity *48*, 399–416.

Wiśniewski, J.R., Zougman, A., Nagaraj, N., and Mann, M. (2009). Universal sample preparation method for proteome analysis. Nat. Methods *6*, 359–362.

Yanovich, G., Agmon, H., Harel, M., Sonnenblick, A., Peretz, T., and Geiger, T. (2018). Clinical Proteomics of breast cancer reveals a novel layer of breast cancer classification. Cancer Res. *78*, 6001–6010.

York, A.G., Williams, K.J., Argus, J.P., Zhou, Q.D., Brar, G., Vergnes, L., Gray, E.E., Zhen, A., Wu, N.C., Yamada, D.H., et al. (2015). Limiting cholesterol biosynthetic flux spontaneously engages type I IFN signaling. Cell *163*, 1716–1729.

Zhang, Y., Kurupati, R., Liu, L., Zhou, X.Y., Zhang, G., Hudaihed, A., Filisio, F., Giles-Davis, W., Xu, X., Karakousis, G.C., et al. (2017). Enhancing $CD8^+$ T cell fatty acid catabolism within a metabolically challenging tumor microenvironment increases the efficacy of melanoma immunotherapy. Cancer Cell *32*, 377–391.

Zhou, F. (2009). Molecular mechanisms of IFN-gamma to up-regulate MHC class I antigen processing and presentation. Int. Rev. Immunol. *28*, 239–260.

Zikich, D., Schachter, J., and Besser, M.J. (2016). Predictors of tumor-infiltrating lymphocyte efficacy in melanoma. Immunotherapy *8*, 35–43.

STAR★METHODS

KEY RESOURCES TABLE

REAGENT or RESOURCE	SOURCE	IDENTIFIER
Antibodies		
Mouse anti-human HLA-DR (clone G46-6) (APC conjugate)	BD Biosciences	Cat#560896; RRID: AB_10563218
Mouse IgG2a κ isotype control (APC conjugate)	BD Biosciences	Cat#551414; RRID: AB_10052279
Mouse anti-human HLA-ABC (clone G46-2.6) (FITC conjugate)	BD Biosciences	Cat#555552; RRID: AB_395935
Mouse IgG1K isotype control (FITC conjugate)	BD Biosciences	Cat#556649; RRID: AB_396513
ACAT1 IHC antibody	Atlas Antibodies	Cat#HPA007569; RRID: AB_1844482
ACOT1 IHC antibody	Atlas Antibodies	Cat#HPA043705; RRID: AB_2678626
HADHA IHC antibody	GeneTex	Cat#GTX113727; RRID: AB_2037134
SDHA IHC antibody	Cell Signaling Technology	Cat#11998; RRID: AB_2750900
FABP7 IHC antibody	Atlas Antibodies	Cat#HPA028825; RRID: AB_10602130
MITF IHC antibody	Cell Marque	Cat#284M-96; RRID: AB_1516912
CD8 IHC antibody	Biocare Medical	Cat#CRM311; RRID: AB_2750579
CD3 IHC antibody	Dako	Cat#A0452; RRID: AB_2335677
H2-kb/H2kd antibody	Biolegend	Cat#114612; RRID: AB_492931
PDL1 antibody	Biolegend	Cat#124314; RRID: AB_10643573
CD4 antibody	BD Biosciences	Cat#564298; RRID: AB_2738734
CD8 antibody	BD Biosciences	Cat#563786; RRID: AB_2732919
CD45 antibody	Biolegend	Cat#103147; RRID: AB_2564383
CD11B antibody	Biolegend	Cat#101226; RRID: AB_830642
F4/80 antibody	Biolegend	Cat#123110; RRID: AB_893486
Ly6C antibody	Biolegend	Cat#128032; RRID: AB_2562178
TNFA antibody	Biolegend	Cat#506306; RRID: AB_315427
IFNG antibody	Biolegend	Cat#505826; RRID: AB_2295770
Biological Samples		
Archival formalin-fixed paraffin-embedded (FFPE) melanoma samples	Sheba Medical Center	N/A
Chemicals, Peptides, and Recombinant Proteins		
Dichloroacetate	Sigma-Aldrich	Cat#347795
Oligomycin	Sigma-Aldrich	Cat#04876
Antimycin A	Sigma-Aldrich	Cat#A8674
Rotenone	Sigma-Aldrich	Cat#R8875
Avasimibe	APEXBIO	Cat#A4318
Etomoxir	Sigma-Aldrich	Cat#E1905
Carbonyl cyanide-p-trifluoromethoxyphenylhydrazone (FCCP)	Sigma-Aldrich	Cat#C2920
Poly-D-Lysine	Sigma-Aldrich	Cat#P1149
Lys-C Mass Spec Grade	Wako Laboratory Chemicals	Cat#125-05061
Sequencing Grade Modified Trypsin	Promega	Cat#V5113
LysC Trypsin mix	Promega	Cat#V5071
Arg10- $^{13}C_6{}^{15}N_4$	Cambridge Isotopes Laboratories	Cat#CNLM-539
Lys8- $^{13}C_6{}^{15}N_2$	Cambridge Isotopes Laboratories	Cat#CNLM-291
SILAC DMEM	Biological Industries	Cat#06-1055-70-1
SILAC RPMI	Biological Industries	Cat#06-1100-28-1
Seahorse XF DMEM	Agilent	Cat#103575

(*Continued on next page*)

Continued

REAGENT or RESOURCE	SOURCE	IDENTIFIER
Bradford reagent	Biorad	Cat#500-0006
Bond Dewax Solution	Leica Biosystems	Cat#LE-AR9222
Bond TM Epitope Retrieval 1	Leica Biosystems	Cat#LE-AR9961
BondTM Wash Solution 10X	Leica Biosystems	Cat#LE-AR9590
BioTri RNA Reagent	Bio-Lab Ltd, Israel	Cat#009010233100
PerfeCTa FastMix II, ROX	Quantabioscience, USA	Cat#84210
Collagenase IV	Sigma-Aldrich	Cat#C5138
DNase I Recombinant	Sigma-Aldrich	Cat#04716728001
PMA	Sigma-Aldrich	Cat#P8139
Ionomycin	STEMCELL Technologies	Cat#73724
Brefeldin A	BD Biosciences	Cat#555029
Critical Commercial Assays		
Pierce BCA Protein Assay Kit	Thermo Scientific	Cat#23225
QScript cDNA Synthesis Kit	Quantabioscience, USA	Cat#95047
MitoTracker® Deep Red FM	Thermo Scientific	Cat#M22426
CytoTox-ONE Homogeneous Membrane Integrity Assay	Promega, USA	Cat#G7891
LIVE/DEAD™ Fixable Red Dead Cell Stain Kit	ThermoFisher	Cat#L23102
Bond Polymer Refine Red Detection Novocastra kit	Leica Biosystems	Cat#DS9390
Seahorse XFe96 FluxPak Kit	Agilent	Cat#102416-100
Deposited Data		
Sample proteomics analysis	PRIDE repository	Project accession: PXD006003
Experimental Models: Cell Lines		
Human: WM266-4 cell line	ATCC	Cat#CRL-1676
Human: WM115 cell line	ATCC	Cat#CRL-1675
Human: A375 cell line	ATCC	Cat#CRL-1619
Human: mel526 cell line	Steven A. Rosenberg's laboratory	N/A
Human: mel624 cell line	Steven A. Rosenberg's laboratory	N/A
Human: mel04 cell line	Ella Institute Labs	N/A
Human: Mel76 cell line	Ella Institute Labs	N/A
Human: TIL14	Ella Institute Labs	N/A
Mouse: YUMMER1.7 (clone D4J)	Yale University School of Medicine	N/A
Experimental Models: Organisms/Strains		
C57BL/6 mouse	Jackson Laboratories	Stock#000664
Oligonucleotides		
See Table S6G for gRNA oligonucleotides	IDT	N/A
See Table S6H for probes and primers for human HLA and control qPCR	Biosearch Technologies, USA	N/A
See Table S6I for mouse qPCR primers	IDT	N/A
Software and Algorithms		
MaxQuant	Cox and Mann, 2008	https://maxquant.org
Andromeda search engine	Cox et al., 2011	N/A
Perseus	Tyanova et al., 2016	https://maxquant.org/perseus
MATLAB	MathWorks	https://www.mathworks.com/products/matlab.html
R Statistical Computing Software	The R Foundation	https://www.r-project.org/
Other		
30 kDa Amicon filters	Millipore	Cat#UFC803024
96-well glass bottom plates	Cellvis, CA, US	Cat#P96-1.5H-N

(*Continued on next page*)

Continued

REAGENT or RESOURCE	SOURCE	IDENTIFIER
Empore Octadecyl C18 47mm Extraction disks	Sigma-Aldrich	Cat#66883-U
Empore Cation 47 mm Extraction Disks	Sigma-Aldrich	Cat#66889-U
Empore Anion SR 47 mm extraction disks	Sigma-Aldrich	Cat#66888-U
50 cm EASY-spray PepMap column	Thermo Scientific	Cat#ES803

LEAD CONTACT AND MATERIALS AVAILABILITY

Further information and requests for resources and reagents should be directed to and will be fulfilled by the Lead Contact, Tamar Geiger (geiger@tauex.tau.ac.il).

Plasmids generated for the study are available from the Lead Contact.

EXPERIMENTAL MODEL AND SUBJECT DETAILS

Tumor sample collection

Archival formalin-fixed paraffin-embedded (FFPE) tissues from 42 metastatic melanoma patients treated with TIL-based adoptive cell transfer were included in this study, 40 which were treated with the "Young TIL" protocol and 2 which were treated with the "Selected TIL" protocol (Besser et al., 2013; Besser et al., 2010). Patients were categorized into 21 responders (complete or partial regression) and 21 non-responders (progressive disease), as evaluated by standard Response Evaluation Criteria In Solid Tumors (RECIST v1.0) guidelines. All patients provided their informed consent according to the Israel Ministry of Health Approval no. 3518/2004. FFPE tissue samples from 74 metastatic melanoma patients treated with anti-PD1 immunotherapy were included in the anti-PD1 cohort. The patients were categorized into 40 responders, 27 non-responders and 7 stable disease patients according to multidisciplinary radiologic evaluations. Samples were taken shortly before the initiation of the indicated treatment (except for 2 samples taken 11 or 18 days after starting treatment). Clinical information of each patient is included in Table S1.

Cell lines

For super-SILAC mix, the following cell lines were cultured in SILAC-medium devoid of lysine and arginine and supplemented with the heavy version of these amino acids. WM266-4, WM115, and A375 were cultured in SILAC-DMEM (Biological Industries) supplemented with 10% dialyzed FBS (Biological Industries), 1 mM sodium pyruvate, 4 mM L-Glutamine, 1% essential amino acids, and antibiotics. Mel526 and Mel624 were cultured in SILAC-RPMI medium (Biological Industries) supplemented with 10% dialyzed FBS (Biological Industries), 1 mM sodium pyruvate, 2 mM L-Glutamine, 25 mmol/l HEPES pH 7.2, and antibiotics. Lys8 concentrations were 73 μg/mL, and Arg10 concentrations were 33.6 μg/mL (for WM266, A375, mel526 and mel624) or 28 μg/mL (for WM115). After 10 doublings, successful incorporation of the labeled amino acids was determined by MS analysis. Cell line authentication for WM266-4, WM115, and A375 was performed at the Genomics Core Facility of BioRap Technologies and the Rappaport Research Institute in Technion, Israel. Short tandem repeat (STR) profiles were determined using the Promega PowerPlex 16 HS kit.

For cell line metabolic and genetic perturbation experiments, WM266-4 cells were cultured in DMEM supplemented with 4 mM L-Glutamine, antibiotics, and 10% FBS. Mel526 cells were cultured in DMEM or RPMI supplemented with 4 mM L-Glutamine, antibiotics, and 10% FBS. Mel76 and Mel04 cells were cultured in RPMI supplemented with 4 mM L-Glutamine, antibiotics, and 10% FBS. YUMMER1.7 (clone D4J) cells were cultured in DMEM F12 supplemented with 4 mM L-Glutamine, antibiotics, 10% FBS, and non-essential amino acids. Cells were treated with the following inhibitors: 30 mM Sodium dichloroacetate (DCA; and PBS as control), 3 μM avasimibe, 100 μM etomoxir, 200 nM rotenone, 250 nM antimycin or 50 nM oligomycin. DMSO treatment was used as vehicle control for all mitochondrial inhibitors. Cells were cultured with each inhibitor / vehicle for 72 h prior to cell lysis or flow cytometry.

Mel76, Mel04 and TIL14 were obtained from surgically excised melanoma specimens (IRB approval no.3518/2004). For the co-culture assay, TIL14 cells were cultured in special TIL medium supplemented as previously described (Besser et al., 2013).

YUMMER1.7 (clone D4J) was generated from YUMM1.7 cells by UV irradiation and single cell clonal selection. The method of generation of the line was previously described (Meeth et al., 2016; Wang et al., 2017b). It was verified as diploid and evaluated for tumor formation in C57BL/6J mice and for response to anti-PD-1 and anti-CTLA-4.

METHOD DETAILS

Proteomics sample preparation

For clinical sample preparation, slides (6-10 μm thick) from FFPE blocks were macro-dissected, deparaffinized with xylene and washed with ethanol. The sample preparation of the TIL cohort was as follows: The extracted tissues were lysed with 4% sodium

dodecyl sulfate (SDS), 0.1 M Tris pH 7.6, and then boiled for 10 min at 95°C, sonicated and centrifuged at 17,000 x g. For super-SILAC standard preparation, the heavy labeled cells were lysed with the same buffer and boiled for 10 min at 95°C. Following protein determination using the BCA protocol (Pierce), the heavy labeled super-SILAC standard lysate and the tumor lysates were mixed at a 1:1 ratio and the total protein lysate was trypsin-digested on 30 kDa filters (Millipore) using the filter-aided sample preparation (FASP) protocol (Wiśniewski et al., 2009). Proteins were denatured on filters in 8 M urea, reduced using 100 mM DTT, and alkylated using 50 mM iodoacetamide, followed by overnight digestion with sequencing grade trypsin (Promega; 1:50 enzyme to protein ratio). Peptides were then acidified with 1% trifluoroacetic acid, separated into six fractions using strong anion exchange (SAX) chromatography in a stage tip format and then purified on C-18 (3M) stage tips (Rappsilber et al., 2003). The sample preparation of the anti-PD1 cohort was as follows: The extracted tissues were lysed with 50% 2-2-2 trifluoroethanol (TFE), 25mM ABC. Samples were boiled for 1 h at 99°C, sonicated and centrifuged at 20,000 x g. Following protein determination using the Bradford protocol, the heavy labeled super-SILAC standard lysate (in the same buffer) and the tumor lysates were mixed at a 1:1 ratio and the total protein lysate was trypsin-digested using in-solution digestion protocol. Proteins were reduced using 5 mM DTT, alkylated with 15 mM iodoacetamide, diluted with 50 mM ammonium bicarbonate followed by overnight digestion with Lys-C-Trypsin mix (1:100 enzyme to protein ratio) and trypsin (Promega; 1:50 enzyme to protein ratio). Peptides were then acidified with 1% trifluoroacetic acid, separated into five fractions using strong cation exchange (SCX) chromatography in a stage tip format and then purified on C-18 (3M) stage tips.

For cell line experiments, cells were lysed upon reaching ~70%–90% confluence using 6 M urea and 2 M thiourea in 50 mM ammonium bicarbonate in at least 3 biological replicates. Protein concentrations were determined using the Bradford assay and the proteins were digested in-solution. Specifically, lysates were reduced with 1 mM DTT, alkylated with 5 mM iodoacetamide, diluted 1:4 with 50 mM ammonium bicarbonate, and digested over-night with Lys-C-Trypsin mix (1:100 enzyme to protein ratio) and trypsin (1:50 enzyme to protein ratio). Next, peptides were acidified with TFA and purified on C-18 stage tips (3M).

LC-MS-based proteomics

LC-MS/MS runs were performed on the EASY-nLC1000 UHPLC (Thermo Scientific) coupled to the Q-Exactive Plus or Q-Exactive HF mass spectrometers (Thermo Scientific) (Scheltema et al., 2014). Peptides were separated with a 50 cm EASY-spray PepMap column (Thermo Scientific) using a water-acetonitrile gradient of 220 min or 140 min for the TIL and the anti-PD1 tumor sample fractions, respectively, with a flow rate of 300 nL/min at 40°C. The gradient for the cell line single shots was 240 min long. Buffer A was 0.1% formic acid, and buffer B was 80% acetonitrile, 0.1% formic acid. For the different SAX fractions of the TIL tumor samples, the gradient was modified according to the pH of the fraction: 5%–25% buffer B (pH 11), 7%–27% buffer B (pH 8, 6 and 5), and 7%–33% buffer B (pH 3 and 4). For the different fractions of the anti-PD1 tumor samples the gradient was modified as follows: 5%–25% for fraction 1-2; 7%–28% for fraction 3-4; 7%–33% for fraction 5. For the cell line single shots, the gradient was 5%–28% or 7%–28% buffer B. The resolutions of the MS and MS/MS spectra were 70,000 and 17,500 for Q-Exactive Plus, respectively. The resolutions of the MS and MS/MS spectra were 60,000 and 30,000 for Q-Exactive HF, respectively. The m/z range was set to 300-1700 or 380-1800 Th. MS data were acquired in a data-dependent mode, with target values of 3E+06 and 1E+05 or 5E+04 for MS and MS/MS scans, respectively, and a top-10 method.

Immunohistochemistry (IHC) staining

FFPE tumor blocks were obtained from the Institute of Pathology at the Sheba Medical Center. For ACAT1, ACOT1, HADHA, FABP7, MITF and SDHA staining, 3.5 μm consecutive sections were mounted on the positively charged glass slides and dried overnight at 37°C. For each protein, 4-5 tumor blocks from the TIL cohort were stained per group (responder / non-responder), except for SDHA (10 slides per group). After deparaffinization and rehydration, staining was performed using BOND-RX automated staining platform (Leica Biosystems), following selected protocol for the Bond Polymer Refine Red Detection Novocastra kit (Leica Biosystems). The kit was selected to ensure proper contrast with endogenous pigmentation. For CD3 and CD8 staining, tissue sections (4 μm) were processed by a fully automated protocol on a Benchmark XT staining module (Ventana Medical Systems Inc., USA). Briefly, after sections were deparaffinized and rehydrated, a CC1 Standard Benchmark XT pretreatment for antigen retrieval (Ventana Medical Systems Inc., USA) was selected for CD3 and CD8. For each protein, 5-6 tissue blocks were stained per group (responder / non-responder). Slides were scanned using the Leica Aperio VERSA Digital Pathology Scanner (Aperio Technologies Inc.). Staining quantification was performed using the Aperio eSlide Manager software via the Aperio Cytoplasmic Algorithm (ACAT1, ACOT1, HADHA, FABP7, MITF and SDHA) or the Aperio Membrane Algorithm (CD3 and CD8 staining). Areas enriched by cancer cells (as defined by a pathologist) were manually annotated and subsequently analyzed by optimized cytoplasm algorithm (Leica Biosystems). Percentage of positively stained cells were used for downstream statistical analysis (Ardiani et al., 2014). The correlation between the different staining was calculated patient-wise using corrplot R code (Pearson correlation analysis).

CRISPR-Cas9 gene knockout

All guide-RNA sequences were selected from the Genescript website and were previously verified (Sanjana et al., 2014). In total 5-6 guide RNAs were examined for each gene, and only those that induced knock out or knock down (as indicated by proteomic analysis) were used. For the human gene knock outs, the gRNAs were cloned into PX459 vector (Addgene plasmid # 62988) (Ran et al., 2013), which contains the Cas9 enzyme from S. pyogenes upstream of the human U6 promoter, a puromycin resistance gene for

mammalian selection and ampicillin resistance gene for bacterial selection. The cloned vectors were sequence verified and transfected into WM266-4 or Mel526 cells at 80%–90% confluence followed by puromycin selection for 2 to 4 weeks. For the murine gene knockout the gRNAs were cloned into PX458-GFP vector, which contains the Cas9 enzyme, U6 promoter, GFP tag and ampicillin resistance gene for bacterial selection. All 6 gRNAs were transfected together into YUMMER1.7 (clone D4J) cells, following selection by flow cytometry. All gene knockouts were confirmed using mass spectrometry analysis. Empty vector without gRNA served at the control.

For Mel526 cells: *ACAT1* KO-1 was derived from *ACAT1* gRNA sequence #3; *ACAT1* KO-2 was derived from *ACAT1* gRNA sequences #1-6; *CPT1A* KO-1 was derived from *CPT1A* gRNA sequences #1-6; *CPT1A* KO-2 was derived from *CPT1A* gRNA sequence #5; *CPT1A* KO-3 was derived from *CPT1A* gRNA sequence #6; *HADHA* KO-1 was derived from *HADHA* gRNA sequence #1; *HADHA* KO-2 was derived from *HADHA* gRNA sequence #2. For WM266-4 cells: *ACAT1* KO-1 was derived from *ACAT1* gRNA sequence #1; *ACAT1* KO-2 was derived from *ACAT1* gRNA sequence #6; *CPT1A* KO-1 was derived from *CPT1A* gRNA sequence #1; *CPT1A* KO-2 was derived from *CPT1A* gRNA sequence #6; *CPT1A* KO-3 was derived from *CPT1A* gRNA sequence #4; *HADHA* KO-1 was derived from *HADHA* gRNA sequence #1; *HADHA* KO-2 was derived from *HADHA* gRNA sequence #2. For YUMMER 1.7 cells: *Acat1* KO was derived from all six *Acat1* gRNA sequences.

T cell killing assay

T cell killing was assayed using LDH cytotoxicity. Briefly, 1×10^4 target cells were co-incubated with effector cells (TIL14) at Effector:Target ratios of 10:1 for 18 h. Cytotoxicity was determined by measuring lactate dehydrogenase (LDH) release with the CytoTox-ONE Homogeneous Membrane Integrity Assay (Promega, USA) according to manufacturer's instructions. Percent of specific killing of target cells was calculated using the equation: (experimental-effector spontaneous release-target spontaneous release) x100 / (target maximum release -target spontaneous release).

Tumor growth assessment and tumor digestion

For tumor growth analysis, 1×10^5 *Acat1*-KO and control YUMMER1.7 (D4J) cell lines were suspended in 100 μL of PBS and then injected subcutaneously into C57BL/6 mice (Jackson Laboratory). All mouse experiments were performed according to approved procedures of the Salk institute of Biological Studies Institutional Animal Care and Use Committee. At indicated time points, *Acat1*-KO and control tumors were collected and minced in HBSS containing collagenase IV (sigma) and DNase (sigma) and digested at 37°C for 30 min. The digested tissues were then filtered, and single cell suspensions were incubated with ACK lysis buffer (Invitrogen) for 2 min to lyse red blood cells. The cells were then re-suspended in complete RPMI for subsequent analyses.

Flow cytometry analysis

For the human cell lines, FACS analysis was performed as follows: Cells were scraped upon reaching up to 90% confluence. Cell pellets were then washed and incubated with HLA antibodies at a 1:10 ratio in FACS buffer containing 1% FBS, 0.1% sodium azide in PBS. Measurements were performed using the Gallios flow cytometer (Beckman Coulter). Three biological replicates were analyzed, each with technical triplicates.

For the YUMMER 1.7 D4J cell line analysis the protocol was performed as follows: *Acat1*-KO and control D4J cells were grown to 70% confluence and scraped using ice-cold PBS. Cell pellets were stained with Live/Dead fixable Red (Invitrogen) followed by surface staining with H2-kb/H2-kd and Pdl1 in FACS buffer (PBS containing 1% FBS, 0.1% sodium azide). For digested tumor samples, single cell suspensions were stained with Live/Dead fixable Red (Thermo Fisher Scientific) in PBS followed by surface staining with antibodies in FACS buffer. For intracellular staining, single cell suspensions were stimulated with PMA (50ng)/Ionomycin (500ng) in the presence of Brefeldin A (BD Biosciences) for 4 h. After fixation and permeabilization, following manufacturer's recommendations, cells were stained for intracellular cytokines. All samples were acquired on a BD LSRII flow cytometer and analyzed with FlowJo software.

RNA expression analysis of MHC class I

For the human cell lines: total RNA was isolated using Tri RNA reagent (Bio-Lab, Israel) according to the manufacturer's instructions. RNA concentration and purity were determined by spectrophotometry and RNA Integrity by electrophoresis. For gene expression analysis 1 μg of total RNA was reverse transcribed using QScript cDNA Synthesis Kit (Quantabioscience, USA) according manufacturer's instructions. The cDNA pools were generated with a QScript cDNA Synthesis Kit (Quantabioscience, USA) according manufacturer's instructions. HLA-A, HLA-B and HLA-C gene expression was measured by real-time PCR using a taqman assay (Biosearch Technologies, USA). All reactions were carried out using the StepOnePlus Real-Time PCR System (Thermo Fisher, USA). The real-time PCR reactions were run in triplicates and normalized to TFRC expression as endogenous control. Relative expression was determined using the $2^{-\Delta\Delta Ct}$ method.

For the YUMMER 1.7 D4J cell line: $3X10^5$ cells were treated with 10 ng/mL IFNγ for 24 h, followed by RNA preparation using RNeasy Plus Mini Kit (QIAGEN). 1μg of total RNA was reverse transcribed using the High Capacity cDNA Reverse Transcription Kit (Thermo Fisher Scientific). 5 ng of cDNA was used to perform qPCR using Fast SYBR Green Master Mix (Thermo Fisher Scientific) and indicated primer on CFX384 Touch Real-Time PCR Detection System (Bio-Rad). Four technical replicates were performed for each biological sample, and expression values of each replicate were normalized against β-Actin cDNA using the $2^{-\Delta\Delta Ct}$ method.

MitoTracker staining and imaging

Mel526 and WM266-4 cell lines were seeded in 96-well glass bottom plates (P96-1.5H-N, Cellvis, CA, USA). A labeling solution of MitoTracker® Deep Red FM (M22426, Thermo Fisher Scientific) was prepared from a 1 mM stock (in DMSO), which was diluted in growth medium to a final concentration of 100 nM. Live cells were stained for 30 min at 37°C, followed by a 5 min wash in PBS. Cells were fixed with 4% paraformaldehyde solution for 15 min at room temperature and washed again for 5 min in PBS. Cells were then stained with DAPI (0.5 μg/mL) for 10 min at room temperature and washed again. Imaging was performed immediately after staining using SP8 inverted confocal microscopy (Leica Microsystems, Wetzlar, Germany) equipped with a Leica HC PL APO CS2c × c63/1.4 NA objective. Excitation and emission ranges: DAPI 405 (415–455), MitoTracker 633 (647–665). 3D reconstructions and deconvolution were performed in LAS-AF software.

Seahorse measurements

WM266-4 or Mel526 CRISPR cells were seeded in a poly-D-lysine-coated XF96 microplate at a density of 20,000 cells per well and incubated at 37°C for 24 h. Basal oxygen consumption rate (OCR), maximal OCR and spare respiratory capacity were measured in the XFe96 Extracellular Flux Analyzer (Seahorse Bioscience, Agilent) using Mito stress assay. For data normalization, cells were fixed and stained using methylene-blue after each experiment.

QUANTIFICATION AND STATISTICAL ANALYSIS

Proteomics raw MS data processing

Raw MS data were processed using MaxQuant version 1.5.2.10 for the TIL dataset and 1.5.6.9 for the anti-PD1 dataset and all the cell line perturbations (Cox and Mann, 2008). Database search was performed with the Andromeda search engine (Cox et al., 2011) using the human Uniprot database. Forward/decoy approach was used to determine the false discovery rate (FDR) and filter the data with a threshold of 1% FDR for both the peptide and the protein levels. The settings included carbamidomethyl cysteine as a fixed modification and methionine oxidation and N-terminal acetylation as variable modifications. The "match between runs" option was enabled to transfer identification between separate LC-MS/MS runs based on their accurate mass and retention time after retention time alignment. The settings for the SILAC-labeled tumor sample runs included Lys-8 and Arg-10 as heavy labels and the re-quantify option was enabled.

Proteomics statistical analysis

All statistical tests and calculations were performed using Perseus (Tyanova et al., 2016), MATLAB, R or Prism. For all proteomic analyses, the proteinGroups output table was used. Reverse proteins, proteins that were only identified by site, and potential contaminants (excluding keratins) were filtered out. For the clinical tumor data, normalized ratio tumor/SILAC data were log2-transformed and the protein groups were filtered to have at least 70% valid values, reaching a list of 4588,4620 or 4416 protein groups for the TIL, the anti-PD1 or the combined datasets respectively, which were further used for all downstream analyses. Dataset integration was based on gene name; multiple entries for the same gene name were integrated to a single entry by calculating the median expression value. Data were normalized by subtracting most frequent value in each sample. To extract DEPs between responders and non-responders multiple comparisons were performed; a two-sample Student's t test was performed with a p value threshold of 0.05 for each of the two datasets, following by 2D annotation enrichment test (Cox and Mann, 2012) with FDR q-value 0.02 to derive the differential functional groups in each of the two datasets. A two-sample Student's t test with a permutation-based FDR q-value of 0.1 and S0 (Tusher et al., 2001) of 0.1 was performed for the anti-PD1 dataset or the combined dataset of both treatments, to extract significantly changing proteins. Enrichment analyses were performed with Fisher's exact test with a FDR q-value < 0.02. Weighted gene co-expression network analysis (WGCNA) was performed on the entire 116 sample dataset using R code implemented in Perseus software using signed network, cor correlation function and power = 10 (Rudolph and Cox, 2019). The Kaplan-Meier survival analyses were performed in MATLAB using log-rank test. Proteomaps were constructed using a web tool based on the t test difference values without log2 transformation (Liebermeister et al., 2014). Protein network was based on a STRING output (Szklarczyk et al., 2017) and was visualized in Cytoscape (Shannon et al., 2003). Principal component analysis was performed after data imputation by replacing missing values with random values that create a normal distribution with a downshift of 1.8 or 1.6 standard deviations and a width of 0.3 or 0.4 of the original ratio distribution for the TIL and the anti-PD1 datasets, respectively. The imputed data were also used for support vector machine (SVM) analyses in Perseus, to find a minimal signature that segregated between responders and non-responders in each dataset. For classification, we used radial basis function (RBF) kernel and feature ranking was performed with ANOVA with S0 of 0.01 or 0.05 for the TIL or anti-PD1 datasets, respectively. Cross-validation was performed by random sampling of 85% of the samples as a training set and testing the classifier on the remaining 15%; this process was repeated 250 times. After protein ranking, the signature was selected based on accuracy (determined according to the area under the ROC curve) of the top-ranked proteins. Accordingly, the top 8-ranked and 15-ranked proteins were selected as the final signatures for the TIL and the anti-PD1 datasets, respectively.

For the cell line metabolic perturbations, label-free quantification normalization data were used after log2 transformation. To find DEPs between DCA-treated and control cells, for each comparison the data were filtered to retain only proteins with valid values in at least 70% of the samples. Following that, two sample Student's t test was performed with a permutation-based FDR q-value

threshold of 0.05 and S0 of 0.1. Integration of multiple t tests was based on gene name; multiple entries for the same gene name were integrated into a single entry by calculating the median expression value. In the CRISPR analysis, for each comparison the data were filtered to retain only proteins with valid values in at least 70% of the samples. Following that, missing data were replaced using imputation based on the assumption of normal distribution with a downshift of 1.6 standard deviations and a width of 0.4 of the original ratio distribution. To find DEPs between CRISPR control and CRISPR KO cells two-sample Student's t test was performed with FDR *q*-value threshold of 0.05 and S0 of 0.1. The following 1D annotation enrichment test was performed on the fold change with Benjamini-Hochberg FDR q value < 0.02. Data integration from multiple t tests was based on gene name; multiple entries for the same gene name were integrated into a single entry by calculating the median expression value.

RNA -sequencing data analysis

Published RNA-sequencing data of anti-CTLA-4 treated patients (Van Allen et al., 2015) was kindly provided by Prof. Schadendorf and Dr. Eliezer M. Van Allen. Published RNA-seq data of anti-PD1 treated patients (Hugo et al., 2016) was downloaded from the GEO database (GEO: GSE78220.) Published RNA-seq data of the TIL dataset (Lauss et al., 2017) was downloaded from the GEO database (GEO; GSE100797). All mRNA data were analyzed using log2 data after filtering for at least 70% valid values. The following gene annotations were added: GOBP, GOMF, GOCC and KEGG. The 2D annotation enrichment test was calculated on the fold change between responders and non-responders in each RNA dataset or proteomics dataset (Benjamini-Hochberg FDR *q*-value < 0.05; one test per RNA dataset).

DATA AND CODE AVAILABILITY

Data resources

The accession number for the MS proteomics data reported in this paper is PRIDE repository: PXD006003.

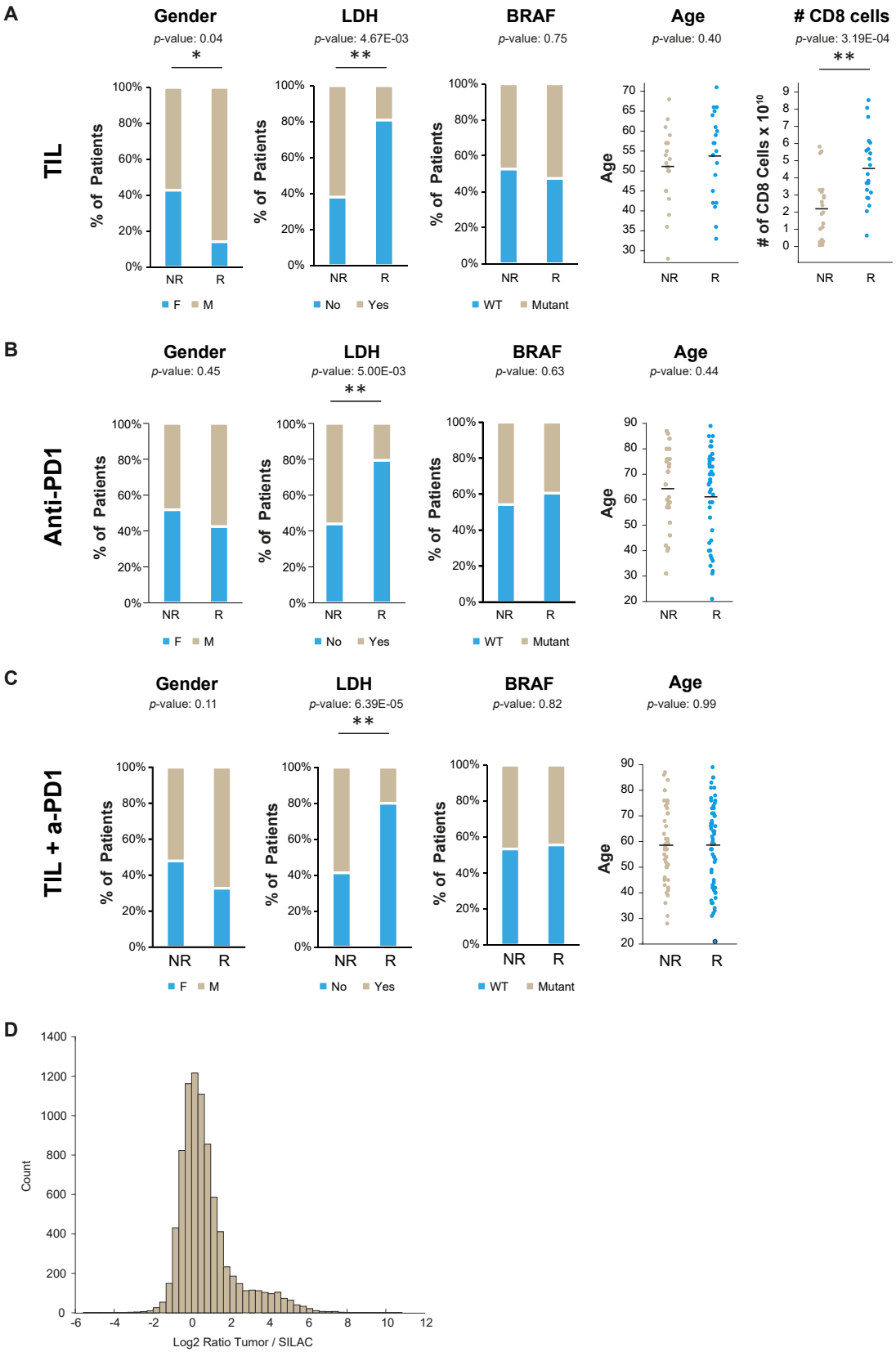

(legend on next page)

Figure S1. Association between Clinical Parameters and Response to Treatments, Related to Figure 1.

The following clinical parameters were examined for the TIL (A), anti-PD1 (B) or combined TIL and anti-PD1 (C) datasets: Gender; lactate dehydrogenase (LDH) levels in the blood; *BRAF* mutational status; age and number of CD8 T cells in the infusion bag (for the TIL patients). *$p < 0.05$; **$p < 0.1$.

(D) Histogram shows overall narrow distribution of ratios toward the super-SILAC standard.

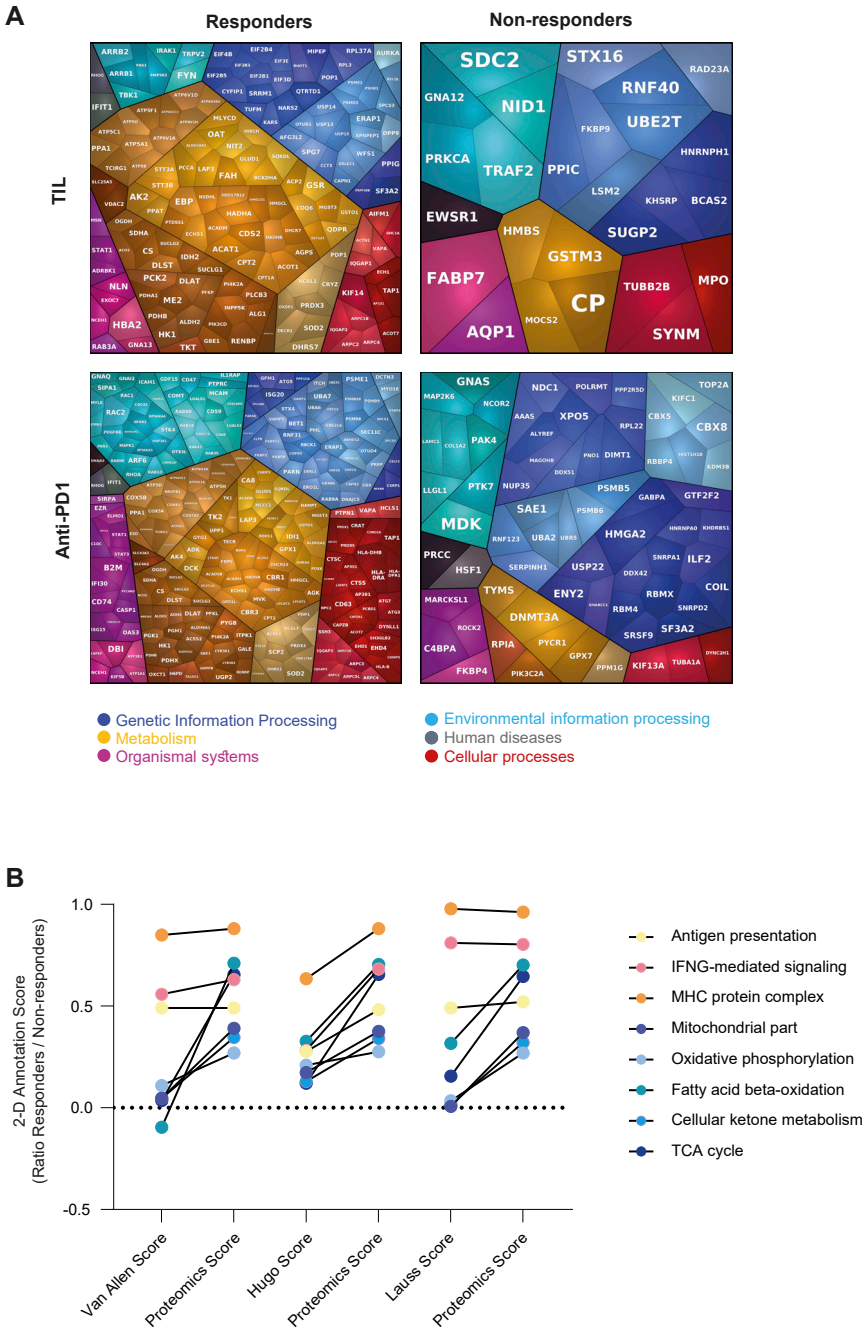

Figure S2. Functional Differences Associated with Response to Immunotherapy, Related to Figure 2.

(A) Functional groups higher in responders (left) and non-responders (right), as illustrated using Proteomaps. Each small polygon corresponds to a single protein that passed the t test, and the size correlates with the ratio between responders and non-responders.

(B) Three 2D annotation enrichment tests (one for each published transcriptomics dataset) compared to the combined proteomics data (FDR q value < 0.05). All of the categories highlighted in the plot are significantly enriched or de-enriched in each dataset. The score indicates enrichment in responders (positive) or non-responders (negative). The proteomic scores of the same category slightly differ as a function of the RNA dataset that it is compared to.

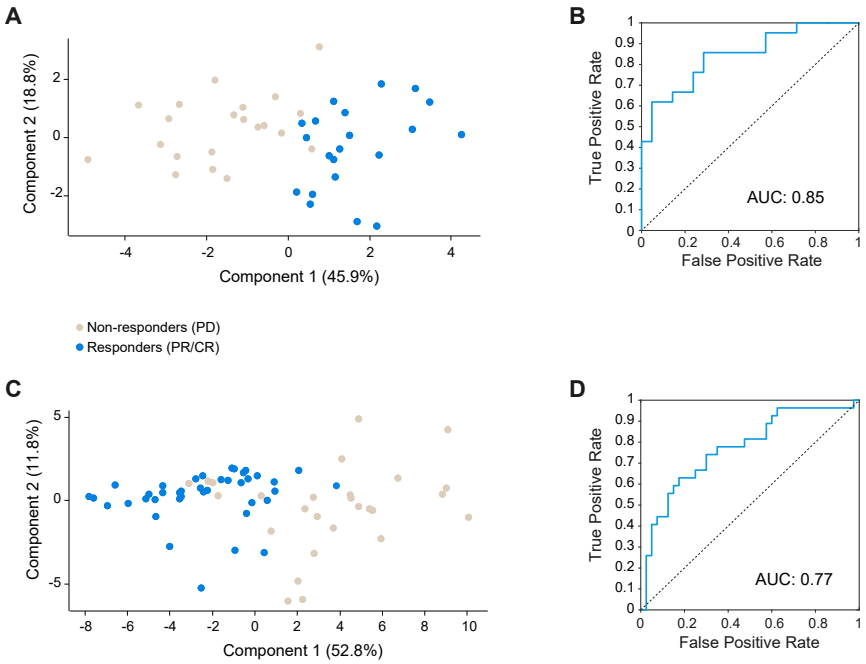

Figure S3. The TIL and Anti-PD1 Signature Proteins Discriminate between Responders and Non-responders, Related to Figure 3.

(A) Principal Component Analysis (PCA) shows good separation between responders and non-responders based on the TIL signature.

(B) Receiver Operating Characteristics (ROC) curve shows high sensitivity and specificity of the TIL signature, with an AUC of 0.85.

(C) PCA shows good separation between responders and non-responders, based on the anti-PD1 signature.

(D) ROC curve shows high sensitivity and specificity of the anti-PD1 signature, with and AUC of 0.77.

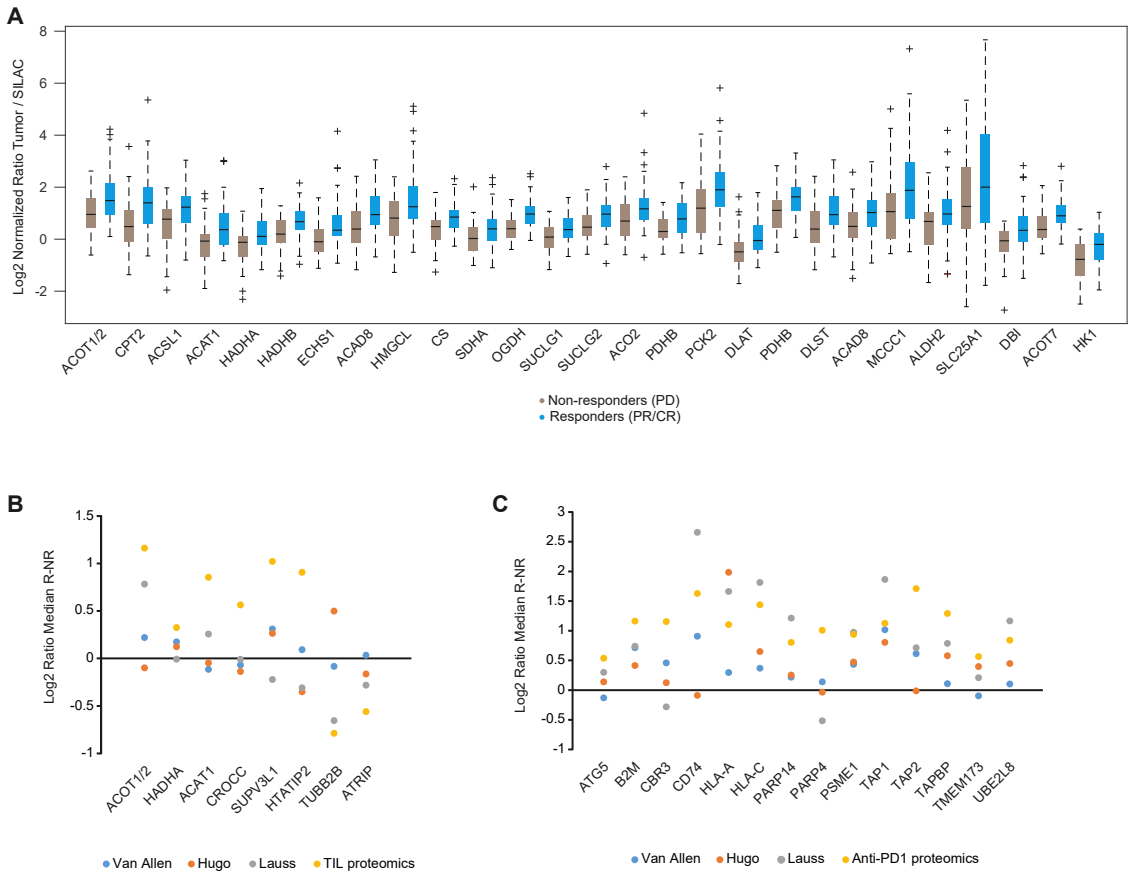

Figure S4. Statistical Analysis of the Integrated PD1 and TIL Cohort and Comparison to RNA Datasets, Related to Figure 4.

(A) Selected examples of metabolic proteins significantly higher in the responder group (combined dataset).

(B and C) Ratio responder/non-responder values of the TIL (B) and anti-PD1 (C) signatures in each of the three examined RNA datasets and the current proteomic dataset.

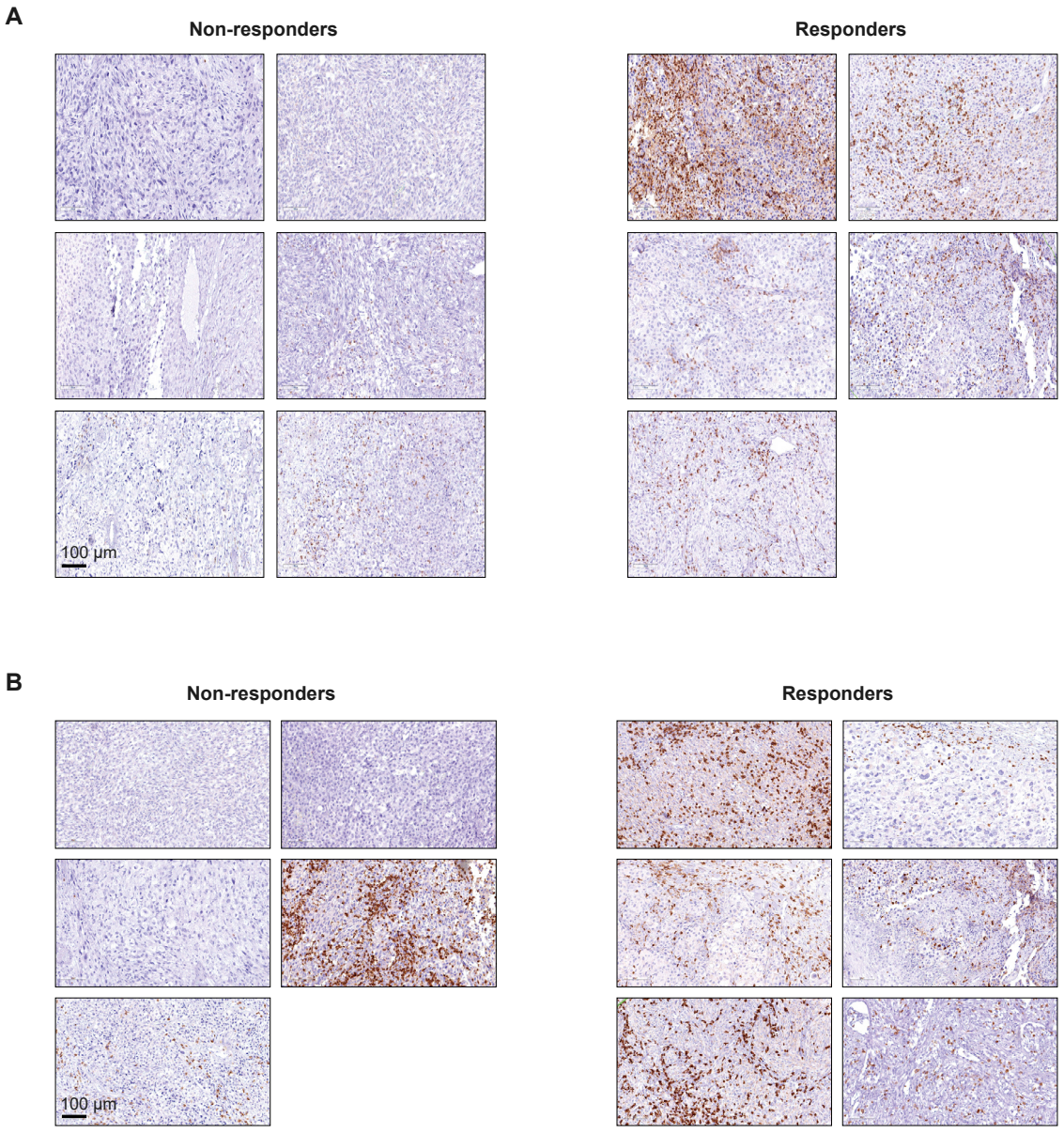

Figure S5. Tissue-Level Examination of T Cell Infiltration, Related to Figure 5.
Immunohistochemistry of CD3 (A) and CD8 (B) cells. The scale bar, 100 μm.

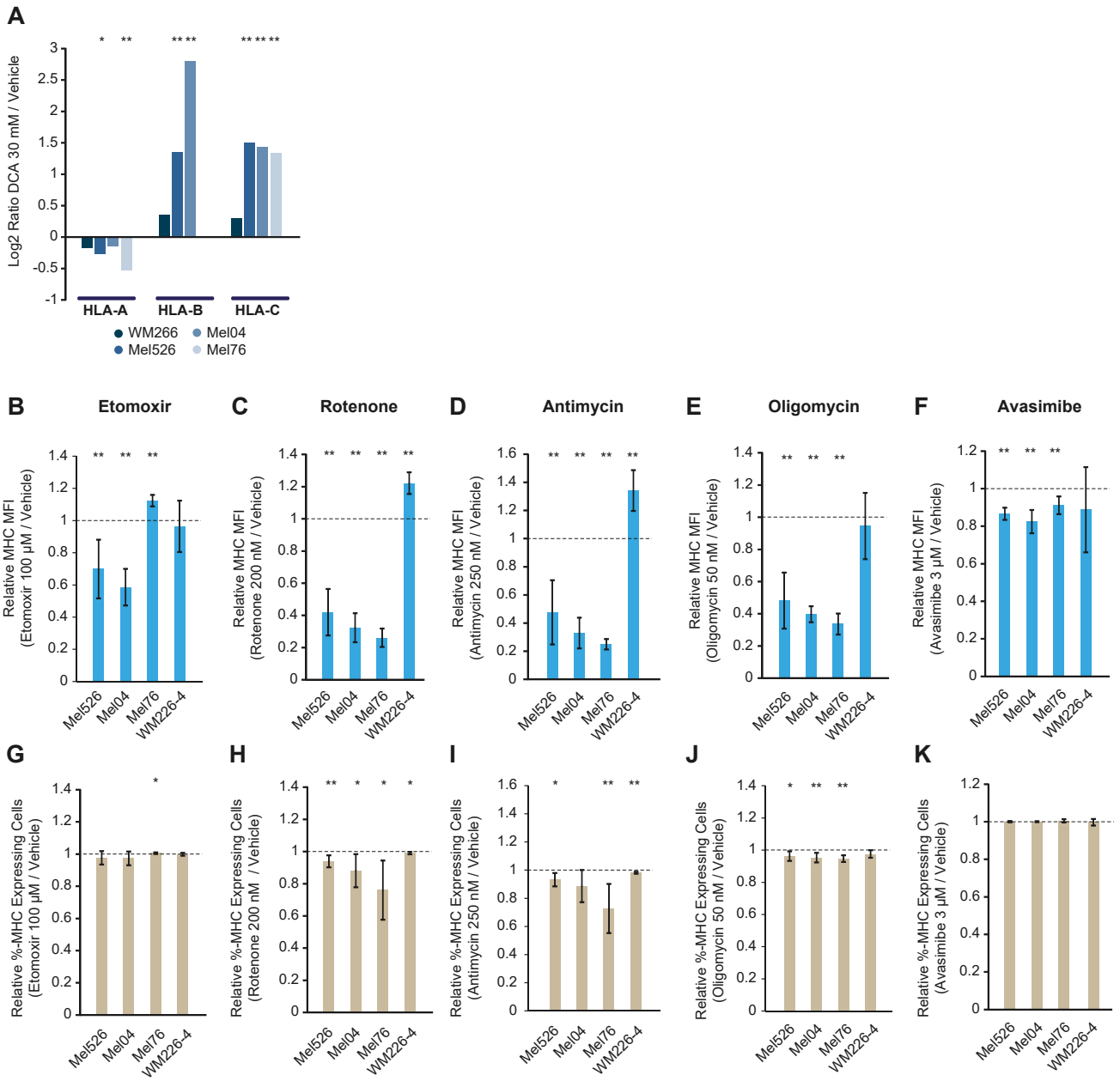

Figure S6. Higher Mitochondrial Activity Is Associated with Higher HLA Expression, Related to Figure 6.

(A) Proteomic analysis of HLA-A, HLA-B and HLA-C in Mel526 and WM266-4 cells treated with 30 mM DCA. Values are log2 ratios of LFQ proteins intensities of treated vs. untreated cells.

(B–K) Flow-cytometry analysis of the change in the HLA-ABC (B–F) or percentage of stained cells (G–K) upon treatment with metabolic drugs: rotenone (B and G), antimycin (C and H), oligomycin (D and I), etomoxir (E and J) and avasimibe (F and K). Data are represented as mean ± SEM. *p < 0.05; **p < 0.1.

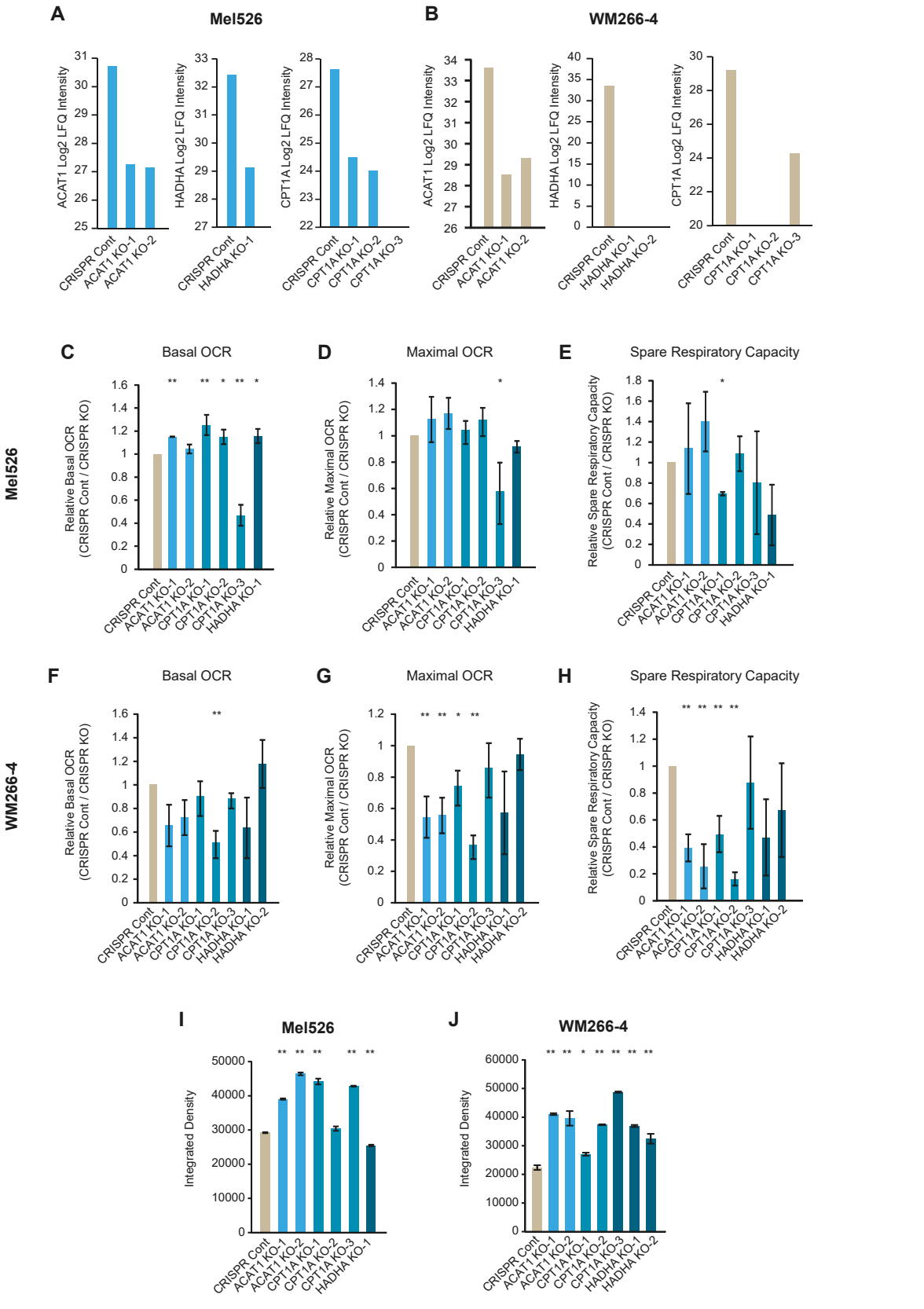

(legend on next page)

Figure S7. Metabolic Analysis of KO Systems, Related to Figure 6.

(A and B) Knock out validation using proteomic analysis in Mel526 (A) and WM266-4 (B).

(C–H) Seahorse measurements of oxygen consumption rate (OCR) in Mel526 (C–E) and WM266-4 (F–H), show basal respiration (C and F), maximal respiration upon treatment with FCCP (D and G) and spare respiratory capacity, which indicates the ability of the cell to respond to increased energy demand or stress (E and H). Data are represented as mean ± SEM. *$p < 0.05$; **$p < 0.1$. (I and J) Mitochondrial mass, as measured by MitoTracker Deep Red staining of Mel526 (I) and WM266-4 (J) cells. Data are represented as mean ± SD. *$p < 0.05$; **$p < 0.1$.

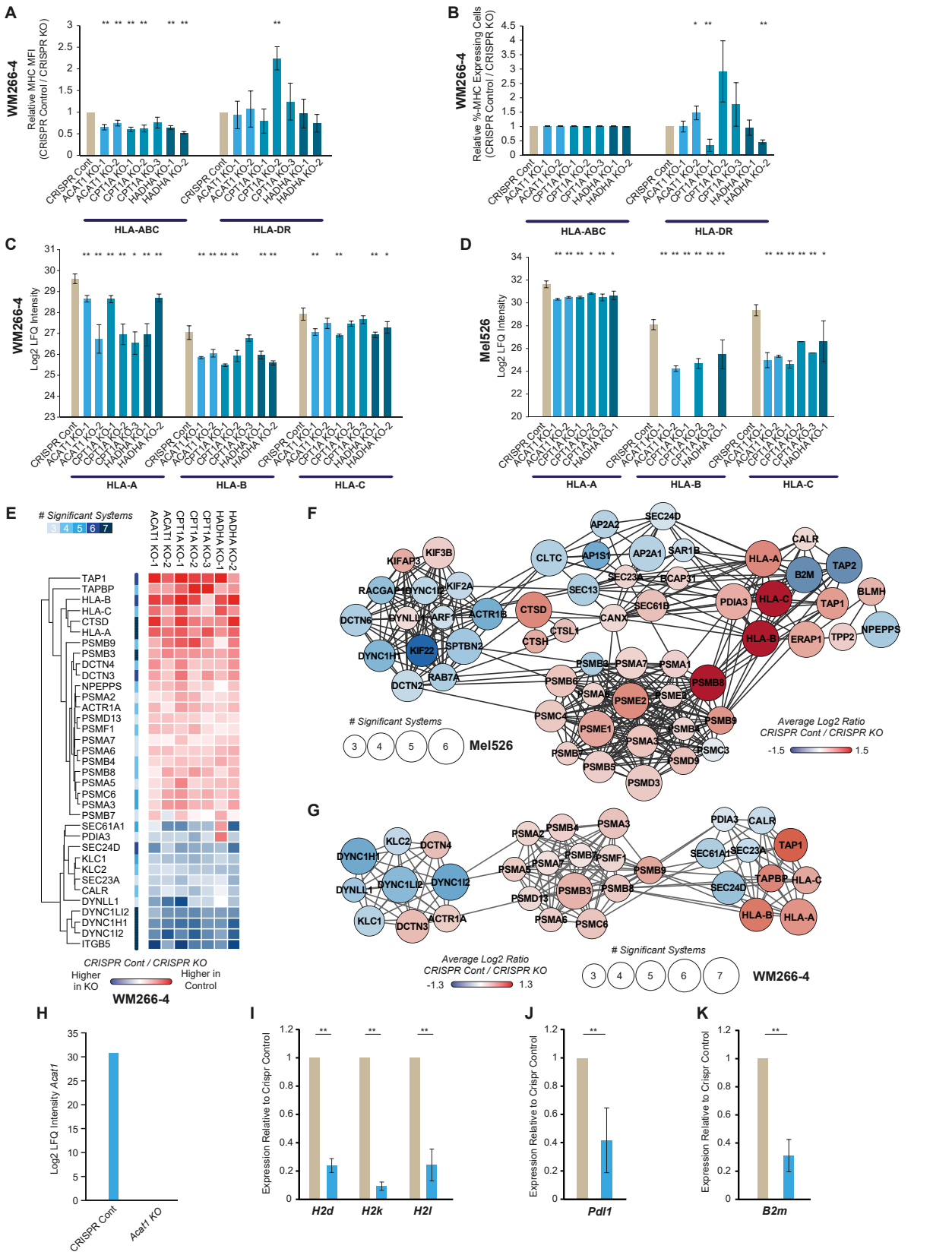

(legend on next page)

Figure S8. Effects of KO Systems on Antigen Presentation and Tumor Immunogenicity, Related to Figure 7.

(A and B) Flow cytometry measurement of the change in HLA-ABC and HLA-DR MFI signal (A) or percentage of stained WM266-4 cells (B). Data are represented as mean ± SEM. *p < 0.05; **p < 0.1.

(C and D) Proteomic analysis of HLA-A, HLA-B and HLA-C in control and KO cells in WM266-4 (C) and Mel526 (D) Values are log2 label free quantification (LFQ) intensity. Data are represented as mean ± SEM. *p < 0.05; **p < 0.1.

(E) Proteomic profile of ''antigen processing and presentation'' (GOBP category) proteins that were significantly different in at least three gene knockouts in WM266-4 (FDR q value<0.05, S0 = 0.1). Values are log2 LFQ intensity ratio of CRISPR control to CRISPR KO.

(F and G) Protein-protein interaction network of the ''antigen processing and presentation'' (GOBP category) proteins that were significantly different in at least three gene knockouts in Mel526 (F) and WM266-4 (G) (FDR q value<0.05, S0 = 0.1).

(H) *Acat1* KO validation by proteomic analysis.

(I–K) Gene expression analysis of MHC class I (I), *Pdl1* (J), and *B2m* (K). All values are relative to untreated CRISPR control cells. Gene expression was normalized relative to actin. Data are represented as mean ± SEM. *p < 0.05; **p < 0.1.